# A comprehensive insight into small system at LHC energies

M.Sc. THESIS

by

Vikrant Sharma (Roll No:- 2103151029)



to

DEPARTMENT OF PHYSICS INDIAN INSTITUTE OF TECHNOLOGY INDORE -  $453\ 552$ , INDIA June, 2023

# A comprehensive insight into small system at LHC energies

#### A THESIS

Submitted in partial fulfilment of the requirements for the award of the degree

 $of \\ {\rm Master~of~Science}$ 

by Vikrant Sharma





# INDIAN INSTITUTE OF TECHNOLOGY INDORE

#### CANDIDATE'S DECLARATION

I hereby certify that the work which is being presented in the thesis entitled A comprehensive insight into small system at LHC energies in the partial fulfillment of the requirements for the award of the degree of Master of Science and submitted in the Department of Physics, Indian Institute of Technology Indore, is an authentic record of my own work carried out during the time period from July 2022 to June 2023 under the supervision of Prof. Raghunath Sahoo, Professor, Indian Institute of Technology Indore.

The matter presented in this thesis has not been submitted by me for the award of any other degree of this or any institute.

Signature of the student with date

(Vikrant Sharma)

This is to certify that the above statement made by the candidate is correct to the best of my knowledge?

Signature of the Supervisor of M.Sc. thesis (with date)

(Prof. Raghunath Sahoo)

Vikrant Sharma has successfully given his M.Sc. Oral Examination held

on 18 May, 2023

Date:

Signature of Supervisor of M. C. thesis

Convener, DPGC

Date: May 23, 2023

( ) I loughit

Signature of PSPC Member no. 1

Signature of PSPC Member no. 2

Date: May 22, 2023 Date: May 23, 2023

#### **ACKNOWLEDGEMENTS**

I would like to take this opportunity to express my deepest gratitude to my supervisor Prof. Raghunath Sahoo for his invaluable guidance, encouragement and unwavering support throughout the course of my master's thesis project. His expertise and insights have been instrumental in shaping this work and have truly been a source of inspiration to me.

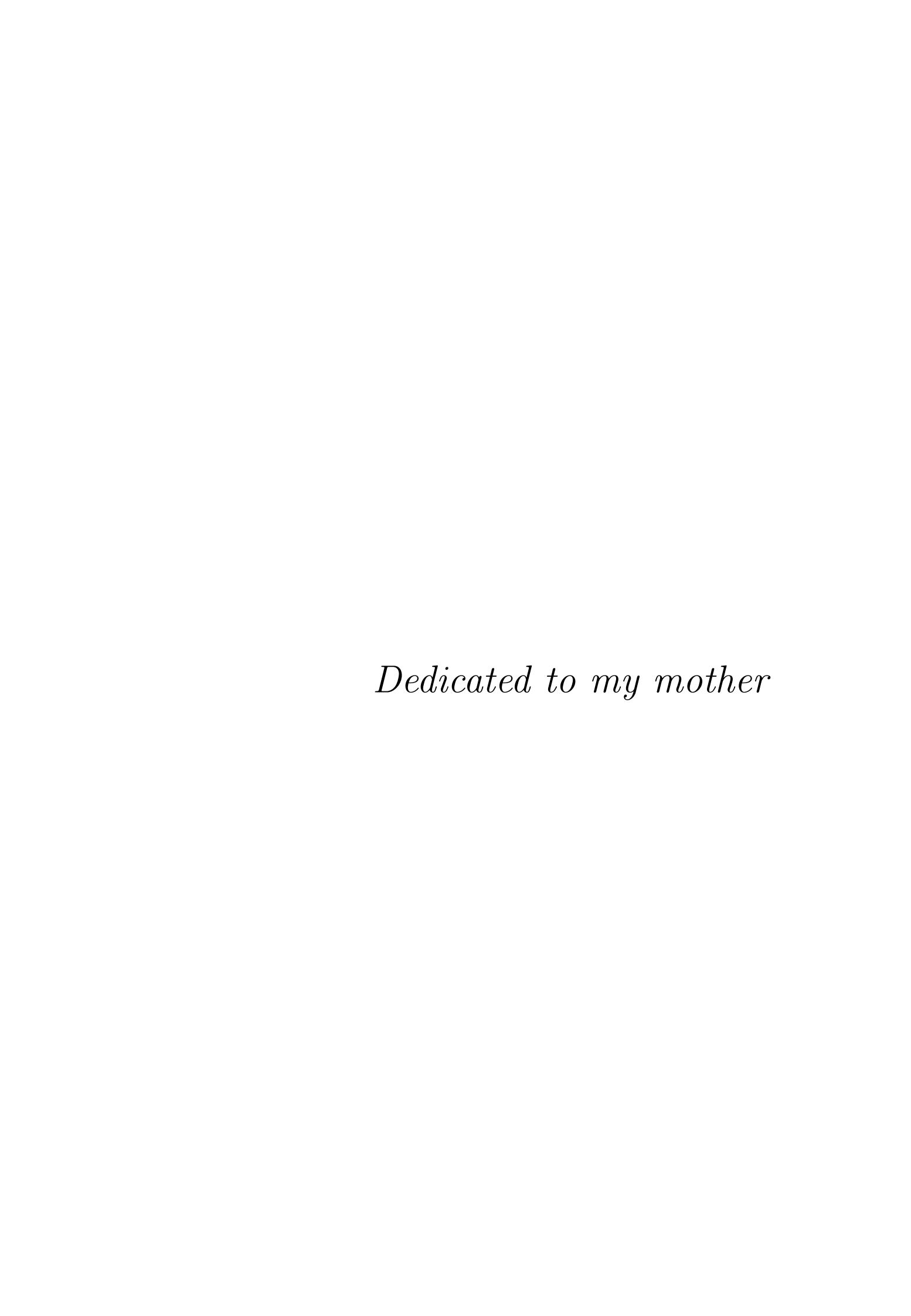
I am also grateful to my PSPC committee members: Prof. Subhendu Rakshit and Dr. Manavendra Mahato for their insightful feedback and valuable inputs that helped me in improving the quality of my research work.

I would also like to extend my sincere thanks to Dr. Suman Deb, Dushmanta Sahu and Ronald Scaria for their guidance and support in providing valuable concepts and fruitful discussions that have helped me in enhancing my research work.

Furthermore, I would like to acknowledge the contributions of Dr. Captain Rituraj Singh and Dr. Jayanta Dey for their valuable insights, and their constant support and motivation.

Last but not least, I am grateful to Suraj Prasad, Neelkamal Mallick, Girija Pradhan, Bhagyarathi sahoo, Kamaljeet singh, Debadatta Behera, Kangkan goswami, Ashwathi menon and Kshitish Pradhan for their constant help and support throughout the project. Their encouragement and support were crucial in keeping me motivated and focused.

In conclusion, this project would not have been possible without the support and guidance of these individuals, and for that, I am truly grateful.



# Contents

1	Intr	roduction	1
	1.1	Relativistic heavy Ion collision	2
	1.2	Relativistic Kinematics	3
		1.2.1 Rapidity	3
		1.2.2 Pseudorapidity	3
		1.2.3 Relation between $\eta$ and y	4
	1.3	Quark Gluon Plasma (QGP)	6
	1.4	Signatures of QGP	9
		1.4.1 New Observation in pp collisions	12
	1.5	Motivation	14
2	Dis	sipative properties	15
	2.1	Formalism	16
3	Me	$\operatorname{ethodology}$	22
	3.1	EPOS-LHC	23
	3.2	Spherocity: A tool to categorize event geometry	28
	3.3	Tsallis statistics	31
4	Res	sults and Discussions	32
	4.1	Tsallis fit for the obtained $p_T$ spectra	33
	4.2	Extracted T, q and R parameters	35
	4.3	Kinetic freeze-out temperature and radial flow strength	37
	4.4	Results: Dissipative properties	39
		4.4.1 Spherocity-wise $k_T$ profile for pions and kaons	39
		4.4.2 Spherocity-wise $\eta/s$ profile for pions and kaons	40

5 Summary and Conclusion			41	
$\mathbf{A}$			43	
	A.1 Spherocity cuts	•	43	
	A.2 Unscaled $p_T$ spectra of pions and kaons	•	44	
	References		45	

# List of Figures

1.1	Relativistic heavy ion collision [1]	2
1.2	Phase diagram of QCD [4]	6
1.3	Schematic representation of the space time evolution of high energy collisions. Compares the system evolution with and without QGP formation [3]	7
1.4	$R_{AA}$ for the inclusive J/ $\psi$ production at plotted as a function of centrality for $\sqrt{s_{NN}}=5.02$ TeV, compared to the results corresponding to $\sqrt{s_{NN}}=2.76$ TeV [10]. Plot is taken from [11]	11
1.5	$p_T$ integrated yield ratios of strange and multi-strange hadrons to pions as a function of mid-rapidity charged particle density. Measurements in pp collisions at $\sqrt{s} = 7$ TeV are compared with results from p-Pb and Pb-Pb collisions and also with theoretical MC models. This shows strangeness enhancement in high-multiplicity $pp$ collisions similar to that	10
1.6	of heavy-ion collisions [3]. Figure is adopted from [13] Two-particle correlation functions for pp at $\sqrt{s}$ = 13TeV [17]	12 13
3.1	Step-by-step procedure followed in this study	23
3.2	This is the schematic depiction of the space-time evolution of particle production in hadronic interaction in EPOS 1.99 or EPOS LHC [36]	25

3.3	charged particle $p_T$ spectra in $pp$ collisions at $\sqrt{s} = 13$ TeV using EPOS-LHC is compared with experimental data from ALICE. The lower panel shows the ratio of both, indicating	
	a nice agreement.	27
3.4	charged particle $\eta$ distribution in $pp$ collisions at $\sqrt{s}=13$ TeV using EPOS-LHC is compared with experimental data from ALICE. The lower panel shows the ratio of both, indicating a nice agreement	27
3.5	Figure showing jetty and isotropic events in the transverse plane. Figure taken from [44]	29
3.6	Spherocity distribution for the mentioned multiplicity classes. $pp$ collisions at $\sqrt{s}=13$ TeV using EPOS-LHC	30
4.1	Fitting of multiplicity-wise $p_T$ spectra of pions and kaon for all three spherocity classes	34
4.2	T for identified particles are shown here from EPOS-LHC data for Spherocity integrated, isotropic and jetty events $(\bullet)$ $S_0$ integrated $(\bullet)$ Isotropic $(\bullet)$ Jetty	35
4.3	R for pion and kaon are shown here from EPOS-LHC data for Spherocity integrated, isotropic and jetty events ( $\bullet$ ) $S_0$ integrated ( $\bullet$ ) Isotropic ( $\bullet$ ) Jetty	36
4.4	Fitting is done using Eq.(4.1) to extract $T_{fro}$ and $\langle u_t \rangle$	37
4.5	$T_{fro}$ and $\langle u_t \rangle$ are extracted using Eq.(4.1) from the EPOS-LHC generated data and are shown in this figure for all three event topologies. ( $\bullet$ ) $S_0$ integrated ( $\bullet$ ) Isotropic ( $\bullet$ ) Jetty	38
4.6	$k_T$ for identified particles are shown here from EPOS-LHC data for Spherocity integrated, isotropic and jetty events ( $\bullet$ )	
	$S_0$ integrated ( $\bullet$ ) Isotropic ( $\bullet$ ) Jetty	39
4.7	$\eta/s$ for identified particles are shown here from EPOS-LHC data for Spherocity integrated, isotropic and jetty events ( $\bullet$ ) $S_0$ integrated ( $\bullet$ ) Isotropic ( $\bullet$ ) Jetty	<i>4</i> ∩
	20 mostace (*) pouropic (*) scory	IU

A.1	Cuts on spherocity are implemented for the classification of	
	jetty and isotropic events	43
A.2	$p_T$ -spectra of pions and kaons from EPOS-LHC for $pp$ at	
	$\sqrt{s} = 13 \text{ TeV for } S_0 \text{ integrated events } \dots \dots \dots$	44

# Chapter 1

# Introduction

Big Bang is the most widely accepted theory about the beginning of the universe. In the very first moments after the big bang the universe existed in an intensely hot and energetic state. It existed for an extremely short duration and contained the building blocks of all matter. As the universe expanded and cooled these combined to produce the matter in the state in which it exists today.

QGP is the state of matter discussed above, it is made up of quarks and gluons. It is obviously impossible for us to go back in time to study the universe in its very early stages but it is possible to mimic the conditions of the early universe by colliding heavy nuclei such as gold or lead, at nearly the speed of light therefore creating a system 10<sup>5</sup> times hotter than the core of the Sun. These extreme conditions are sufficient for the possible formation of QGP.

ALICE (A Large Ion Collider Experiment) is one of the four major experiments at LHC (Large Hardon Collider) dedicated to studying the above mentioned collisions which usually occur at GeV and TeV energies.

To study the QCD matter at extreme temperatures and energy densities (where QGP is expected to form) the LHC accelerates ions to make them collide at the centre of mass energy upto  $\sqrt{s_{NN}} = 5.02$  TeV per nucleon pair. This energy is expected to be high enough to heat up the system above the critical temperature required for QGP formation, therefore allowing hadrons to undergo a transition into a deconfined state of quarks

## 1.1 Relativistic heavy Ion collision

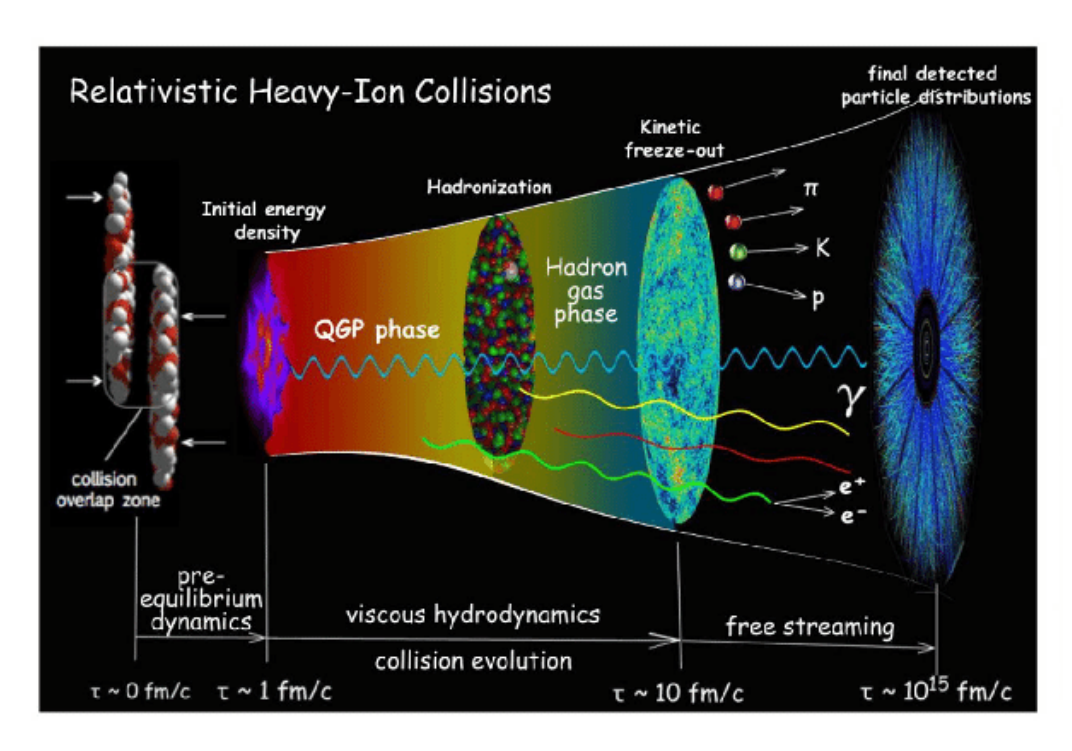


Figure 1.1: Relativistic heavy ion collision [1].

To clearly understand the state of matter and its behaviour in the early universe, physicists have taken advantage of nuclear and hadronic collisions at ultra-relativistic speeds. At the LHC, the energy of the colliding particles is of the order of TeV. With the availability of such high energies, the temperature of produced matter increases to such a value that the gluons and quarks become deconfined, this particular deconfined state of gluons and quarks is known as Quark gluon plasma (QGP).

As these collisions take place at relativistic speeds, it becomes important to understand the relativistic kinematics and a few of the widely used basic terms such as rapidity and pseudorapidity.

## 1.2 Relativistic Kinematics

### 1.2.1 Rapidity

As the velocity is not additive in the regime of relativistic velocities, a new quantity is constructed which is linearly additive, termed as rapidity.

$$y = \frac{1}{2} \ln \left( \frac{1+\beta}{1-\beta} \right) \tag{1.1}$$

The relation between rapidity y of a particle in the laboratory frame is related to its rapidity y' in a boosted Lorentz frame which is moving with a velocity  $\beta$  in the specified z-direction is given as:

$$y' = \frac{1}{2} \ln \left( \frac{p'_0 + p'_z}{p'_0 - p'_z} \right) \tag{1.2}$$

We know that under the Lorentz transformation the energy component of four-momentum and its z-component in some frame F are related to their respective components in a boosted lorentz frame F'.

$$p_0' = \gamma(p_0 - \beta p_z) \tag{1.3}$$

$$p_z' = \gamma(p_z' - \beta p_0) \tag{1.4}$$

Here,  $\beta$  is the velocity of F' with respect to F. Substituting Eq.(1.4) and eq.(1.4) in Eq.(1.2), we finally get the formula for rapidity, given as;

$$y' = \frac{1}{2} \ln \left[ \frac{\gamma (1 - \beta)(p_0 + p_z)}{\gamma (1 + \beta)(p_0 - p_z)} \right]$$
 (1.5)

$$= y - \frac{1}{2} \ln \left( \frac{1+\beta}{1-\beta} \right) \tag{1.6}$$

## 1.2.2 Pseudorapidity

It is clear from Eq.(1.2) that to determine rapidity we need the information of  $p_0$  and  $p_z$  and it is experimentally difficult to determine these variables, but it is possible to approximate Eq.(1.2) in high energy cases  $(\mathbf{p} >> m)$  to a form which is only one variable dependent, this particular

quantity is known as pseudorapidity.

$$\eta = -\ln\left[\tan(\theta/2)\right] \tag{1.7}$$

Here,  $\theta$  is the angle made of the momentum of particle  $\vec{\mathbf{p}}$  with the beam axis. In terms of  $\mathbf{p}$ ,  $\eta$  variable can be expressed as

$$\eta = \frac{1}{2} \ln \left( \frac{|\mathbf{p}| + p_z}{|\mathbf{p}| - p_z} \right) \tag{1.8}$$

### 1.2.3 Relation between $\eta$ and y

By the comparison of Eqs.(1.1) and (1.8), it can easily be seen that at large momentum ( $|\mathbf{p}| \approx p_0$ ) the pseudorapidity and rapidty variable coincides.

$$e^{\eta} = \sqrt{\frac{|\mathbf{p}| + p_z}{|\mathbf{p}| - p_z}} \tag{1.9}$$

$$e^{-\eta} = \sqrt{\frac{|\mathbf{p}| - p_z}{|\mathbf{p}| + p_z}} \tag{1.10}$$

by the addition of above two equations we can obtain the relation

$$|\mathbf{p}| = p_T \cosh \eta$$

and by subtraction of Eq.(1.10) from (1.9), we can obtain

$$p_z = p_z \sinh \eta$$

where  $p_T$  is the magnitude if transverse momentum

$$p_T = \sqrt{\mathbf{p}^2 - p_z^2}$$

By using the above results, we can write the rapidity variable in terms

of the pseudorapidity variable as

$$y = \frac{1}{2} \ln \left[ \frac{\sqrt{p_T^2 \cosh^2 \eta + m^2} + p_T \sinh \eta}{\sqrt{p_T^2 \cosh^2 \eta + m^2} - p_T \sinh \eta} \right]$$
(1.11)

If the particle distribution is expressed as  $d^2N/dyd\mathbf{p}_T$  in the terms of y, then in terms of  $\eta$  the particle distribution is

$$\frac{d^2N}{d\eta d\mathbf{p}_T} = \sqrt{1 - \frac{m^2}{m_T^2 \cosh^2 y}} \frac{d^2N}{dy d\mathbf{p}_T}$$
(1.12)

From Eq.(1.12), it can be inferred that in the region of y >> 0,  $dN/d\eta$  and dN/dy are almost equal but in the region  $y \approx 0$ , there is a small dip in the  $dN/d\eta$  distribution as compared to dN/dy distribution. Experimentally it is easy to measure the angle of outgoing particle with respect to beam axis but it is difficult to measure all the components of the four-momentum. So it becomes preferable to express all distributions in terms of  $\eta$ .

## 1.3 Quark Gluon Plasma (QGP)

The strange property of "asymptotic freedom and infrared slavery" [2] of QCD suggest that it is impossible to observe free partons, still there have been attempts to create a plasma of these partons. QGP is locally thermally equilibrated strongly interacting phase of quarks and gluons which can possibly be created in the laboratory by colliding two Lorentz contracted heavy nuclei at relativistic energies. This can possibly be achieved by raising the temperature of the nuclei up to the range of few hundreds of MeVs (achieved at RHIC and LHC energies) or can be achieved by diffusing hadronic boundaries by compression of nuclei [3].

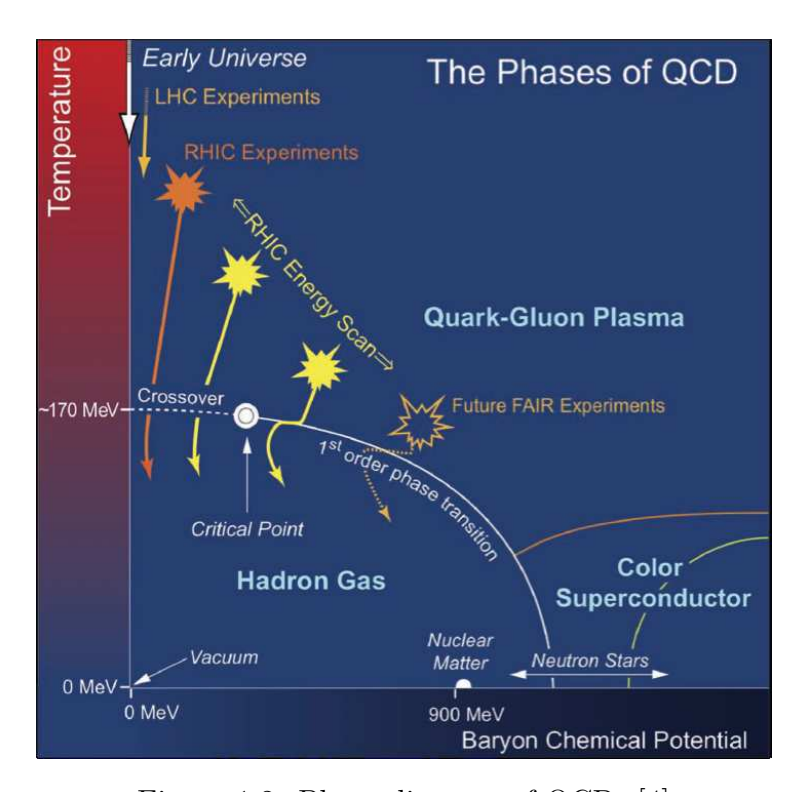


Figure 1.2: Phase diagram of QCD [4]

In Fig.(1.2), various phases of QCD have been depicted in a plot in which the temperature (T) has been plotted as a function of baryon chemical potential ( $\mu_B$ ). Some stellar objects like neutron stars belong to the region of low temperature and high baryon chemical potential whereas the early universe is usually imagined to have a extremely high temperature and zero baryon chemical potential. RHIC and LHC experiments are able to produce such high temperatures creating the suitable conditions for the possible formation of QGP.

In such experiments, after a collision at relativistic energies of nuclei, series of processes possibly lead to formation of QGP and eventually hadronization. The space-time evolutions (shown in Fig.(1.3)) in hadronic and heavy-ion collisions involves various degree of freedoms at different space-time coordinates [3].

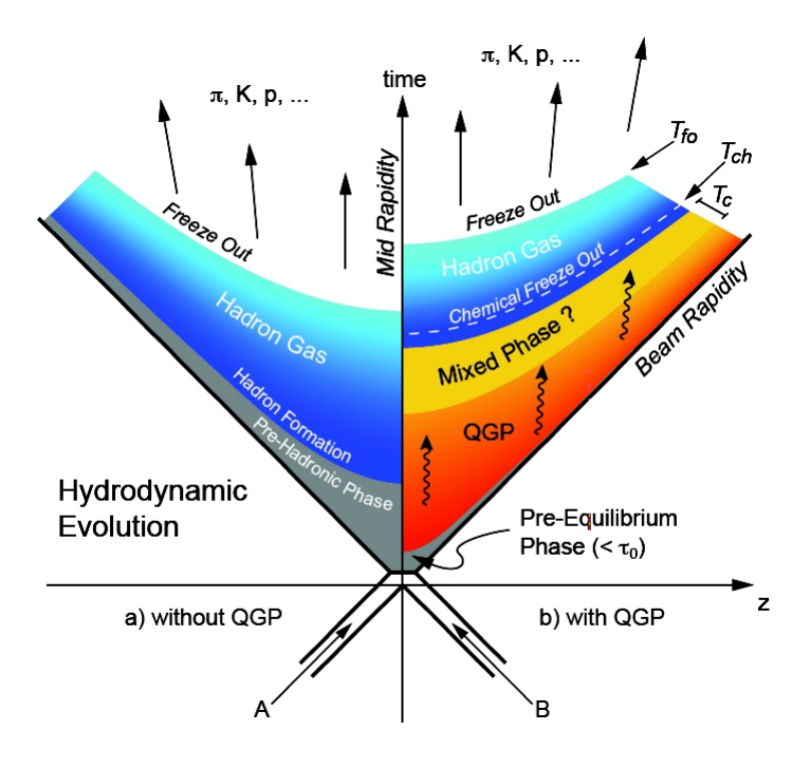


Figure 1.3: Schematic representation of the space time evolution of high energy collisions. Compares the system evolution with and without QGP formation [3].

- Pre-equilibrium stage: When two Lorentz contracted nuclei collide with each other, energy is deposited and a large number of partons (quarks and gluons) are produced, leading to the inelastic interactions among them, thus forming the pre-equilibrium phase.
- Formation of QGP and its evolution: In the overlap region of two colliding nuclei, the constituents undergo multiple rescatterings due to a smaller mean free path as compared to system size, therefore, driving the system towards thermalization. When energy density becomes sufficiently high and at time  $\tau = \tau_0$  the system attains thermal

equilibrium therefore resulting in the formation of QGP. Using the laws of relativistic hydrodynamics the evolution of QGP can be explained.

- Chemical Freeze-out: When energy density begins to drop below the critical value required for the QGP formation the quarks and gluons start to form hadrons. These hadrons inelastically interact to produce new particles. The particular stage at which the inelastic collisions cease to exist is called chemical freeze-out (CFO) and the temperature corresponding to this stage is called freeze-out temperature  $(T_{ch})$ .
- Kinetic Freeze-out: Even though the production of new particles is stopped, these particles can still elastically interact with each other thus changing the momentum distribution and when the mean free path becomes greater than the size of the system elastic interaction is also ceased and the momentum distribution of these particles is fixed. The temperature corresponding to this stage is the kinetic freeze-out temperature  $(T_{kin})$ .

## 1.4 Signatures of QGP

As it is known that the QGP is very short-lived so it is not possible to probe its existence directly through experiments. The only way to examine QGP is to develop observables which can be experimentally measured and the information about QGP is indirectly extracted. Few of the signatures of QGP such as strangeness enhancement, dileptons and photons, jet quenching,  $J/\Psi$  suppression are briefly discussed here.

- Strangeness enhancement: Enhancement in the production of strange particles in the final yield in heavy-ion (AA, 'A' is the heavy-ion nucleus) collisions in contrast to pp and pA collisions is considered to be an important probe of QGP [5]. There is no strange quark in the initial colliding nuclei. Strange quark pair production is more favourable in parton-parton interaction than hadronic interactions. In the QGP phase, the temperature of the medium is greater than the mass of the strange quark so as a consequence of this, strange quarks and anti-quarks production takes place which leads to strangeness enhancement. Strangeness enhancement is observed experimentally in heavy ion collisions at SPS [6], LHC [7] and RHIC [8] energies. These experiments have energies ranging from GeV to TeV scale.
- Jet Quenching: At relativistic hadronic or nuclear collisions, very high- $p_T$  particles are formed because of the initial partonic interactions [3]. High  $p_T$  quarks and gluons are produced from partonic scatterings, these fragments create a multitude of correlated particles in the conical volume called "jets" [3]. Hard partons are produced early (formation time  $\tau \sim \frac{1}{p_T}$ ) and therefore serve as a probe for the study of early stages of collisions [3]. Eventually, these jets lose energy while traversing through high-density medium and this energy loss is path length dependent. This resultant attenuation of the coming out jet structure is known as "Jet Quenching". Jet quenching is measured via an observable called nuclear modification factor and is

an important probe for QGP medium formation. The nuclear modification factor quantifies the amount of suppression in jet yields in nucleus-nucleus collision with respect to pp collision and is defined as:

$$R_{AA}(p_T) = \frac{1}{\langle N_{coll} \rangle} \frac{\left(\frac{d^2 N_{ch}}{d\eta dp_T}\right)_{AA}}{\left(\frac{d^2 N_{ch}}{d\eta dp_T}\right)_{pp}}$$

where  $\langle N_{coll} \rangle$  is the mean number of binary nucleon-nucleon collision occurring in single nucleus-nucleus collision and  $d^2N_{ch}/d\eta dp_T$  is the yield. It is usually obtained from the estimations of Glauber model [9].

#### • $J/\Psi$ Suppression:

" $J/\Psi$ " is a bound state of charm and anti-charm quark and it is formed in the initial hard scattering. In the QGP medium, due to the presence of various quarks and gluons, a charm quark may not come in vicinity of an anti-charm quark (or vice-versa) to form a bound state, this phenemenon is called color Debye screening. In pp collisions, it is believed that no medium is formed (QGP), so the charm and anti-charm can easily combine to form  $J/\Psi$ , whereas, in case of heavy-ion collision there is a possible formation of a thermalized medium (QGP) due to which Debye screening occurs and the production of  $J/\Psi$  is suppressed.  $J/\Psi$  suppression was first proposed in 1986 by Matsui and Satz [12]. At very high temperatures the string tension between charm and anti-charm vanishes. Also due to the Debye screening yields of open charms  $(D^0, D^{\pm} \text{ etc})$  are enhanced since the unbounded charm quarks can possibly combine with nearby light flavors [3]. It is also possible that a large number of charm and anti-charms are formed in the system if the collision energy is sufficiently high. This can possibly create a competetion between suppression and regeneration/recombination and due to this reason the  $J/\Psi$  suppression is less in LHC heavy-ion collisions in comparison

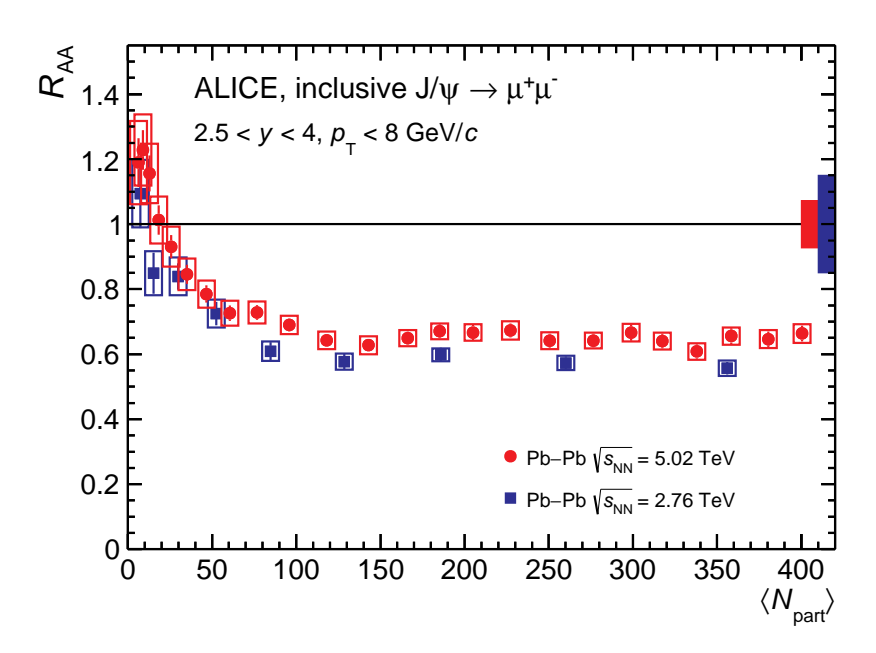


Figure 1.4:  $R_{AA}$  for the inclusive J/ $\psi$  production at plotted as a function of centrality for  $\sqrt{s_{NN}} = 5.02$  TeV, compared to the results corresponding to  $\sqrt{s_{NN}} = 2.76$  TeV [10]. Plot is taken from [11].

with RHIC heavy-ion collision [3].

### 1.4.1 New Observation in pp collisions

pp collisions are usually treated as the baseline for measurements in the search for QGP in heavy-ion collisions. The formation of QGP is generally associated with heavy-ion collisions at ultra-relativistic speeds but some new experimental observations for high multiplicity pp at TeV energies have strongly suggested the possible formation of QGP droplets.

#### **Enhancement of Multi-strange Particles**

ALICE experiment has studied the multi-strange particles production enhancement in pp collisions (at  $\sqrt{s}$  =7 TeV) of high-multiplicity at midrapidity (rapidity is  $y = \frac{1}{2} \ln \frac{E+P_z}{E-P_z}$ ) [13]. Ratio of  $p_T$  integrated yields of multistrange particles with respect to pions is taken as the measure of strangeness production. It is noted that pp collisions (high multiplicity) show similar values as that of heavy-ion collisions (Pb-Pb) [13].

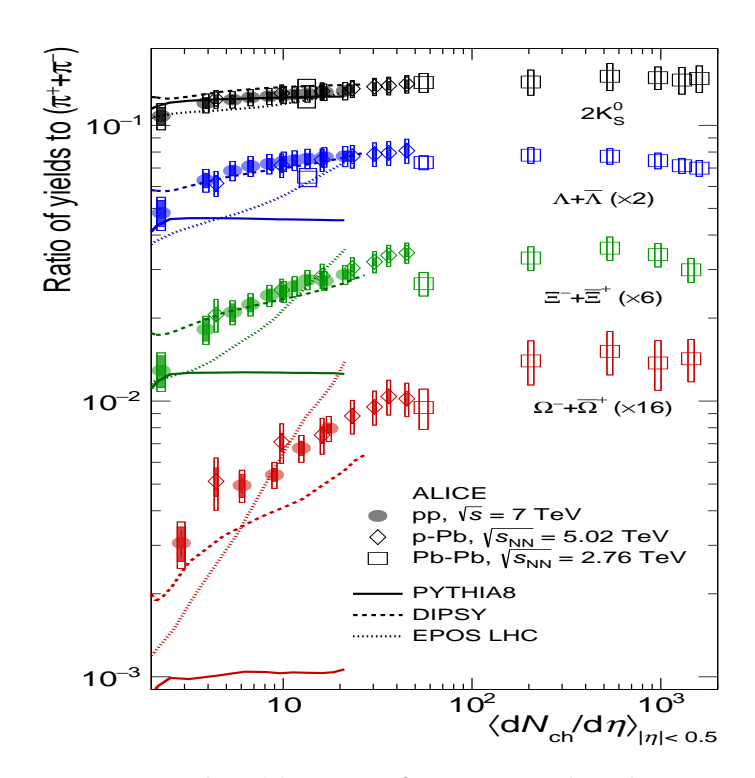


Figure 1.5:  $p_T$  integrated yield ratios of strange and multi-strange hadrons to pions as a function of mid-rapidity charged particle density. Measurements in pp collisions at  $\sqrt{s} = 7$  TeV are compared with results from p-Pb and Pb-Pb collisions and also with theoretical MC models. This shows strangeness enhancement in high-multiplicity pp collisions similar to that of heavy-ion collisions [3]. Figure is adopted from [13].

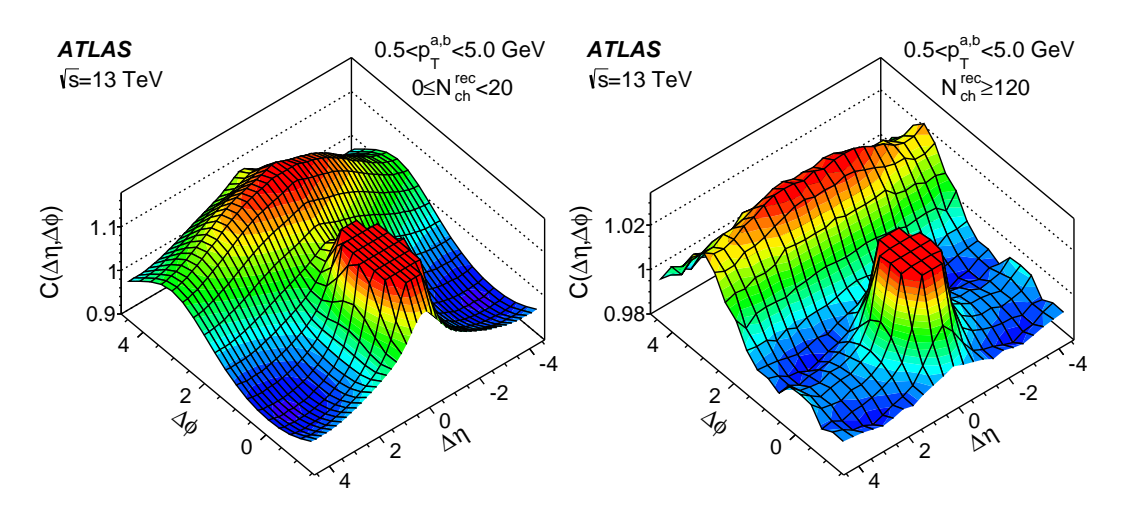


Figure 1.6: Two-particle correlation functions for pp at  $\sqrt{s}$ = 13TeV [17]

#### Collectivity and Multiparticle Ridge-like correlations

In case of pp collisions at LHC energies, the  $p_T$  spectra can be well explained by the Tsallis-Levy function. Low- $p_T$  part of spectra is taken to obtain the collective radial flow velocity of system. For pp collisions at 7 TeV using such analysis on multi-strange particle spectra gives  $T_{fo} = 163 \pm 10 \text{MeV}$  and  $\langle \beta \rangle = 0.49 \pm 0.02$  [14], where  $T_{fo}$  is kinetic freeze-out temperature and  $\langle \beta \rangle$  is radial flow velocity, this obtained temperature remarkably falls within the temperature range which is required for the deconfinement transition as per the lattice QCD estimates [15]. It is also noted that high-multiplicity pp events show a high degree of collectivity too.

Long range near-side structure in two particle azimuthal correlations is known as "ridge". It has been observed in Au-Au [14] and Cu-Cu collisions at RHIC and in Pb-Pb collisions at LHC. Ridge formation in heavy systems is explained by the hydrodynamic collective flow of strongly interacting matter undergoing expansion. CMS experiment at LHC has observed [16] a similar ridge like structure ( $\Delta \phi \sim 0$ ) in the two particle correlations produced in high multiplicity pp collisions. Along with many other observations, this has opened up a new direction in the understanding of particle production in case of small systems (like pp collisions).

## 1.5 Motivation

The observations discussed in the previous section make the high multiplicity pp systems intriguing since such systems point towards the possible presence of a thermalized medium (QGP) which puts in question on the treatment of pp as the baseline for heavy-ion collisions. This motivates us to apply a hydrodynamics-inspired model to study the evolution of systems formed in high multiplicity pp collisions. Since the said system may be QGP-like, which is believed to be a perfect fluid so it becomes interesting to study the properties such as shear viscosity  $(\eta)$  and isothermal compressibility  $(k_T)$ . These dissipative quantities explicitly depend on the thermodynamics of the medium. That medium can be at equilibrium or away from it, to treat both the medium behaviour through a single formulation we have considered the Tsallis distribution function to obtain  $\eta$  and  $k_T$ . This Tsallis distribution is used to fit the particle spectra available at kinetic freeze-out. From fitting the spectra we obtain the kinetic freeze-out temperature. However, Tsallis being an empirical relation the temperature obtained through this also has a radial flow component. It is also possible to obtain a common kinetic freeze-out temperature without radial flow component [18]. The temperature obtained with these methods can be used to estimate the dissipative properties of the medium at the kinetic freeze-out, which is essentially an artifact of the initial thermodynamics. Further, it is investigated in various studies that kinetic-freeze out temperature depends on the event geometry. On the basis of the difference in thermodynamics involved in different event geometry, it is reported in the Ref. [19], that jetty events can be disentangled from the isotropic ones. This motivates us to study the dissipative properties for different event shape geometry separately. So, the objective of this study is to find the common freeze-out temperature, the strength of average radial flow, isothermal compressibility and shear viscosity for different multiplicity classes and event geometries.

# Chapter 2

# Dissipative properties

The isothermal compressibility ( $k_T$ ) and shear viscosity ( $\eta/s$ ) are the useful thermodynamic quantities which give us the information about the behaviour of system.

At the RHIC, the measurements of elliptic flow from heavy-ion collisions have concluded that the medium formed in these ultra-relativistic collisions have a  $\eta/s$  close to the KSS bounds [1], suggesting that QGP almost behaves as a perfect fluid [20], [21]. Therefore, in order to understand the fluidity of the medium formed we must study  $\eta/s$ .

Similarly,  $k_T$  is used to quantify the change in volume of the formed medium with respect to pressure at a constant temperature [22]. Therefore, it helps us to measure the deviation of a fluid from a perfect fluid. The system is incompressible when its  $k_T = 0$ , which makes the system a perfect fluid. A recent finding has shown that QGP has the lowest estimated  $k_T$  till now, so it behaves nearly as a perfect fluid [23].

Speed of sound has a crucial role in having a complete understanding of the equation of state of the system. It helps us to understand the hydrodynamic evolution of the formed matter since it affects the final state momentum distribution. It is concluded from observations that the speed of sound  $(c_s^2)$  is different in various phases, namely the QGP phase, mixed phase and hadronic phase. The value of  $c_s^2$  is 1/3 for the case of non-interacting massless gas, while its value is 1/5 for a hadron gas [24].

## 2.1 Formalism

In this study, the approach mentioned in [25] is used to calculate the dissipative properties such as shear and bulk viscosity for a hadronic matter using non-extensive statistics. We start with the Boltzmann transport equation which is given by,

$$\frac{\partial f_p}{\partial t} + v_p^i \frac{\partial f_p}{\partial x^i} + F_p^i \frac{\partial f_p}{\partial p^i} = I(f_p), \tag{2.1}$$

where  $v_p^i$  refers to the velocity of  $i^{\text{th}}$  particle and  $F_p^i$  corresponds to the external force which is acting on  $i^{\text{th}}$  particle. When the system approaches q-equilibrium, the rate of change of non-equilibrium distribution function is given by the collision integral  $I(f_p)$ .

If no external force is assumed along with the relaxation time approximation then the collision integral can be approximated as,

$$I(f_p) \simeq -\frac{(f_p - f_p^0)}{\tau(E_p)},$$
 (2.2)

where  $\tau(E_p)$  is the collision time (otherwiser known as relaxation time). A non-extensive Tsallis distribution is taken as  $f_p^0$  [26] in the proximity of the fluid's local rest frame, where T,  $\mu_B$  and fluid velocity,  $\mathbf{u}$ , which varies slowly in space and time [27] locally desribes the system, . The thermodynamically consistent Tsallis distribution,  $(f_p^0)$  [28] in the Boltzmann's approximation is given as,

$$f_p^0 = \frac{1}{\left[1 + (q-1)\left(\frac{E_p - \mathbf{p.u} - \mu}{T}\right)\right]^{\frac{q}{q-1}}}$$
(2.3)

where **u** is the fluid velocity. T and  $\mu$  are temperature and chemical potential, respectively.  $\mu = b\mu_B + s\mu_s$ , where b and s are baryon and strangeness quantum numbers, respectively.  $\mu_B$  and  $\mu_s$  are baryon and strange chemical potentials. Strangeness neutrality condition is not considered here for simplicity.

Now, the stress-energy tensor  $(T^{\mu\nu})$  can be written as,

$$T^{\mu\nu} = T_0^{\mu\nu} + T_{dissi}^{\mu\nu},\tag{2.4}$$

where  $T_0^{\mu\nu}$  and  $T_{dissi}^{\mu\nu}$  are the ideal part and the dissipative part respectively (of the stress-energy tensor). When QCD is described hydrodynami-cally, shear and bulk viscosities go into the dissipative part of the stress-energy tensor. In the local lorentz frame, it can be expressed as [27],

$$T_{dissi}^{ij} = -\eta \left( \frac{\partial u^i}{\partial x^j} + \frac{\partial u^j}{\partial x^i} \right) - \left( \zeta - \frac{2}{3} \eta \right) \frac{\partial u^i}{\partial x^j} \delta^{ij}. \tag{2.5}$$

Also in the terms of distribution function, this can also be written as,

$$T_{dissi}^{ij} = \int \frac{d^3p}{(2\pi)^3} \frac{p^i p^j}{E_p} \delta f_p, \qquad (2.6)$$

where  $\delta f_p$  is the measure of deviation of the distribution function from the q-equilibrium and it is expressed as (from Eqs. 2.1 and 2.2),

$$\delta f_p = -\tau(E_p) \left( \frac{\partial f_p^0}{\partial t} + v_p^i \frac{\partial f_p^0}{\partial x^i} \right). \tag{2.7}$$

If a steady flow is assumed (of the form  $u^i = (u_x(y), 0, 0)$ ) along with the assumption of a space-time independent temperature, Eq. 2.5 simplifies to  $T^{xy} = -\eta \partial u_x/\partial y$ . Now, from Eqs. 2.6 and 2.7, we get (using  $\mu = 0$ ),

$$T^{xy} = \left\{ -\frac{1}{T} \int \frac{d^3p}{(2\pi)^3} \tau(E_p) \left( \frac{p_x p_y}{E_p} \right)^2 q(f_p^0)^{\frac{(2q-1)}{q}} \right\} \frac{\partial u_x}{\partial y}.$$
 (2.8)

Therefore, for a single component of hadronic matter, the corresponding shear viscosity can be written as,

$$\eta = \frac{1}{15T} \int \frac{d^3p}{(2\pi)^3} \tau(E_p) \frac{p^4}{E_p^2} q(f_p^0)^{\frac{(2q-1)}{q}}.$$
 (2.9)

At finite chemical potential, the shear viscosity of a multi-component

hadron gas are expressed as [29],

$$\eta = \frac{1}{15T} \sum_{a} \int \frac{d^3p}{(2\pi)^3} \frac{p^4}{E_a^2} q \left( \tau_a(f_a^0)^{\frac{(2q-1)}{q}} + \bar{\tau_a}(\bar{f_a^0})^{\frac{(2q-1)}{q}} \right), \tag{2.10}$$

Here  $E_a^2 = p^2 + m_a^2$  and the antiparticles are represented by the barred quantities. For the  $a^{\rm th}$  particle,  $f_a^0$  is the distribution function. Now, the energy dependent relaxation time is given as,

$$\tau^{-1}(E_a) = \sum_{bcd} \int \frac{d^3 p_b d^3 p_c d^3 p_d}{(2\pi)^3 (2\pi)^3 (2\pi)^3} W(a, b \to c, d) f_b^0, \tag{2.11}$$

where  $W(a, b \to c, d)$  is the transition rate defined as,

$$W(a, b \to c, d) = \frac{2\pi^4 \delta(p_a + p_b - p_c - p_d)}{2E_a 2E_b 2E_c 2E_d} |\mathcal{M}|^2.$$
 (2.12)

Here  $|\mathcal{M}|$  is the transition amplitude. Eq. 2.11 can be further simplified in the center-of-mass frame as [29],

$$\tau^{-1}(E_a) = \sum_b \int \frac{d^3 p_b}{(2\pi)^3} \sigma_{ab} \frac{\sqrt{s - 4m^2}}{2E_a 2E_b} f_b^0$$

$$\equiv \sum_b \int \frac{d^3 p_b}{(2\pi)^3} \sigma_{ab} v_{ab} f_b^0,$$
(2.13)

where  $v_{ab}$  refers to the relative velocity and  $\sqrt{s}$  is the center-of-mass energy.  $\sigma_{ab}$  corresponds to the total scattering cross-section in the process  $a(p_a) + b(p_b) \rightarrow a(p_c) + b(p_d)$ . To further simplify,  $\tau(E_a)$  is approximated to averaged relaxation time ( $\tilde{\tau}$ ) [30] and by averaging over  $f_a^0$  it can be estimated from Eq. 2.13 as,

$$\widetilde{\tau_a}^{-1}(E_a) = \frac{\int \frac{d^3 p_a}{(2\pi)^3} \tau^{-1}(E_a) f_a^0}{\int \frac{d^3 p_a}{(2\pi)^3} f_a^0} 
= \sum_b \frac{\int \frac{d^3 p_a}{(2\pi)^3} \frac{d^3 p_b}{(2\pi)^3} \sigma_{ab} v_{ab} f_a^0 f_b^0}{\int \frac{d^3 p_a}{(2\pi)^3} f_a^0} 
= \sum_b n_b \langle \sigma_{ab} v_{ab} \rangle,$$
(2.14)

here  $n_b = \int \frac{d^3p_b}{(2\pi)^3} f_b^0$  corresponds to the number density of  $b^{th}$  hadronic species. At zero baryon density the thermal average for the scattering of particles of same species with a constant cross-section can be calculated as follows [25], [31], [32].

$$\langle \sigma_{ab} v_{ab} \rangle = \frac{\sigma \int d^3 p_a d^3 p_b v_{ab} e_q^{-E_a/T} e_q^{-E_b/T}}{\int d^3 p_a d^3 p_b e_q^{-E_a/T} e_q^{-E_b/T}}.$$
 (2.15)

Here  $e_q^{(x)}$  is the q-exponential which is defined as  $e_q^{(x)} = [1 + (q-1)x]^{q/(q-1)}$ . The volume elements in momentum space are expressed as,

$$d^3p_ad^3p_b = 8\pi^2 p_a p_b dE_a dE_b d\cos\theta. \tag{2.16}$$

The numerator in Eq. 2.15 is written as,

$$\sigma \int d^{3}p_{a}d^{3}p_{b}v_{ab}e_{q}^{-E_{a}/T}e_{q}^{-E_{b}/T} = \sigma \int 8\pi^{2}p_{a}p_{b}dE_{a}dE_{b}d\cos\theta \ e_{q}^{-E_{a}/T}e_{q}^{-E_{b}/T} \times \frac{\sqrt{(E_{a}E_{b} - p_{a}p_{b}\cos\theta)^{2} - (m_{a}m_{b})^{2}}}{E_{a}E_{b} - p_{a}p_{b}\cos\theta} (2.17)$$

and the denominator is written as,

$$\int d^{3}p_{a}d^{3}p_{b}e_{q}^{-E_{a}/T}e_{q}^{-E_{b}/T} = \int 8\pi^{2}p_{a}p_{b}dE_{a}dE_{b} \times d\cos\theta e_{q}^{-E_{a}/T}e_{q}^{-E_{b}/T}.$$
(2.18)

Now, in the case of generalized Tsallis non-extensive statistics for q-equilibrium, the  $\langle \sigma_{ab} v_{ab} \rangle$  takes the following form,

$$\langle \sigma_{ab} v_{ab} \rangle = \frac{\sigma \int 8\pi^2 p_a p_b dE_a dE_b d\cos\theta \ e_q^{-E_a/T} e_q^{-E_b/T} \times \frac{\sqrt{(E_a E_b - p_a p_b \cos\theta)^2 - (m_a m_b)^2}}{E_a E_b - p_a p_b \cos\theta}}{\int 8\pi^2 p_a p_b dE_a dE_b d\cos\theta \ e_q^{-E_a/T} e_q^{-E_b/T}}$$
(2.19)

Here  $\sigma$  refers to the cross-section in the case of hadronic collision, for the purpose of calculations it is taken as a constant of value 11.3 mb [25], [29].  $E_a$  and  $E_b$  are integrated in the limit  $m_a$  to  $\infty$  and  $m_b$  to  $\infty$ , respectively. The calculation of relaxation time is done by using Eqs. 2.14 and 2.19. In non-extensive statistics, the other important thermodynamical quantities such as number density (n), energy density  $(\epsilon)$  and pressure (P) are calculated as [28],

$$n = g \int \frac{d^3p}{(2\pi)^3} \left[ 1 + (q-1)\frac{E-\mu}{T} \right]^{-\frac{q}{q-1}}$$
 (2.20)

$$\epsilon = g \int \frac{d^3 p}{(2\pi)^3} E \left[ 1 + (q-1) \frac{E-\mu}{T} \right]^{-\frac{q}{q-1}}$$
 (2.21)

$$P = g \int \frac{d^3p}{(2\pi)^3} \frac{p^2}{3E} \left[ 1 + (q-1)\frac{E-\mu}{T} \right]^{-\frac{q}{q-1}}.$$
 (2.22)

The non-extensive entropy density, s can be calculated from the above expression as,

$$s = \frac{\epsilon + P - \mu n}{T}. (2.23)$$

In our study we have used the basic equation for entropy addition (while estimating for the multi-component hadron gas) in the case of non-extensive statistics, this equation is given by,

$$s(A+B) = s(A) + s(B) - (q-1)s(A)s(B), (2.24)$$

here s(A + B) is the total entropy of A and B. The entropies of A and B are denoted by s(A) and s(B), respectively.

We have also estimated the isothermal compressibility for hadron gas using non-extensive statistics. The isothermal compressibility  $(\kappa_T)$  is

defined as [33],

$$\kappa_T = -\frac{1}{V} \left( \frac{\partial V}{\partial P} \right)_T, \tag{2.25}$$

where V corresponds to the volume of system. Also, the isothermal compressibility can be described in terms of fluctuation and average number as [33], [34],

$$\langle (N - \langle N \rangle)^2 \rangle = var(N) = \frac{T \langle N \rangle^2}{V} \kappa_T.$$
 (2.26)

As we have used the thermodynamically consistent Tsallis statistics, the above mentioned thermodynamical relation is valid in this particular case. By implementing the basic thermodynamical relation  $\langle (N-\langle N\rangle)^2 \rangle = VT\frac{\partial n}{\partial \mu}$ , Eq. 2.26 can further be described in terms of number density and compressibility as,

$$\frac{1}{\kappa_T} = \sum_{a} \frac{n_{aq}^2}{\left(\frac{\partial n_{aq}}{\partial \mu}\right)},\tag{2.27}$$

where  $\frac{\partial n_q}{\partial \mu}$  is given as,

$$\frac{\partial n_q}{\partial \mu} = \frac{gq}{T} \int \frac{d^3p}{(2\pi)^3} \left[ 1 + (q-1)\frac{E-\mu}{T} \right]^{\frac{1-2q}{q-1}}.$$
 (2.28)

In our study, we have implemented the above-discussed formalism to obtain the  $k_T$  and  $\eta/s$ . The inputs of the above formalism are temperature and the non-extensive parameter, which we have obtained by fitting Tsallis function on the obtained multiplicity-wise  $p_T$  spectra for pions and kaons for all three cases of event geometries.

# Chapter 3

# Methodology

As discussed previously, several interesting observations for high multiplicity pp collisions raise a question on the baseline treatment of pp collisions for heavy-ion collisions because these observations point towards the possible formation of a thermalized medium in high multiplicity ppcollisions. Based on these observations it becomes desirable to apply a hydrodynamics-inspired model to study various properties of such collisions, one such model is EPOS. It is also discussed in previous studies [19] that high multiplicity pp collisions are dominated by isotropic events and also that there is a difference in thermodynamics involved in events with different spherocity classes. So we have used the EPOS-LHC model for the purpose of involving the hydrodynamic evolution in our study. We have extracted the T and q parameters by fitting the Tsallis under the hydrodynamics limit, for the sake of visualisation of  $p_T$  spectra for pions and kaons we have shown their respective multiplicity-wise spectra in Appendix A. We have also implemented event geometry classification so that a distinction in thermodynamics and dissipative properties can be done on the basis of event geometry. The various steps of this study are shown in Fig. (3.1) below.

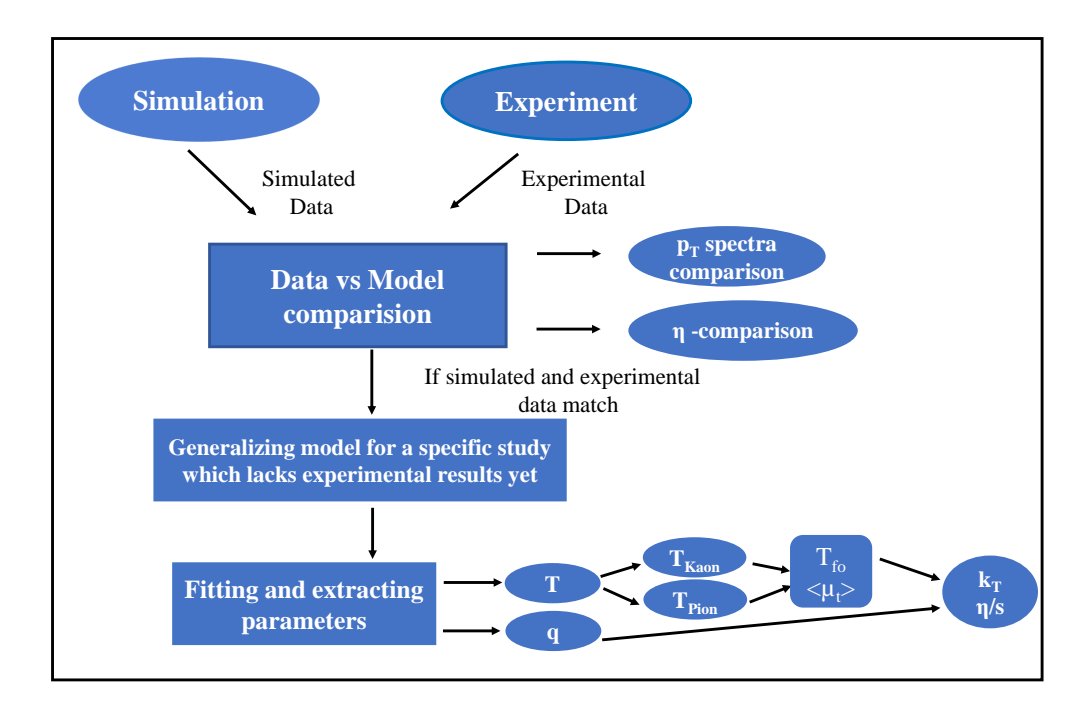


Figure 3.1: Step-by-step procedure followed in this study

#### 3.1 EPOS-LHC

#### Basic features of EPOS 1.99

AA ( and also pp ) collisions amount to numerous parallel collisions of elementary particles. This elementary scattering is known as the "parton ladder", it is also referred to as cut Pomeron [35].

The parton ladder is the representation of parton evolutions from the projectile and the target side towards the centre (small x) [36]. It has already been established that the parton ladder may be considered as a quasi-longitudinal colour field which is known as a "flux tube" [37] and it is conveniently treated as a relativistic string.

It is worthwhile to note that in EPOS the initial conditions for hadronization are not based on partons, rather they are based on strings. The "initial conditions" refers to the system's state after the initial and final state radiation of jets when partons hadronize in HEP models and before the possible hadron or parton rescattering like in HI collisions(final state interactions) [36]. The formation of initial strings is caused by the initial scatterings, which then break into segments, usually identified with hadrons. Then a

situation is considered at an early  $\tau_0$  (proper time), which is long before the formation of hadrons: the distinction between string segments in the dense region (higher than some critical density  $\rho_0$  segments per unit volume) and segments in low-density region are done. The region with high and low density is referred to as core and corona respectively [38]. The corona is important for aspects like the centrality dependence of all observables in HI collisions. Here it corresponds to the unmodified string fragmentation (just like usual models of HEP) and it dominates at the large  $\eta$  and in events with low multiplicity. The most unique and significantly important feature of EPOS is the core since it provides several fascinating effects which are not considered in other HEP models (which are all "corona"-like) [36]. The core is formed of various clusters in each  $\eta$  bin to keep the distribution of local energy density and hadronization of each cluster is done via a microcanonical procedure with an additional radial and longitudinal flow exactly explained in [38]. Energy, flavours and momentum are perfectly conserved by this procedure [36].

For each of the above-mentioned clusters, its mass M is defined as

$$M = \sqrt{(\Sigma_i E_i)^2 - (\Sigma_i \vec{P_i})^2}$$
(3.1)

where the index i ranges over all the segments which forms the cluster and  $(E_i, \vec{P_i})$  is the segment's four-momentum vector. Event-by-event a particular part of string segments normally hadronizes (corona) and the other part is used to generate a core with a collective hadronization as depicted in Fig.(3.2). If the local string segment density is sufficiently high enough, then only the core appears. This limit is easily achieved in the case of central heavy ion collisions at LHC or RHIC because of the large number of nucleon pairs undergo inelastic interaction [36].

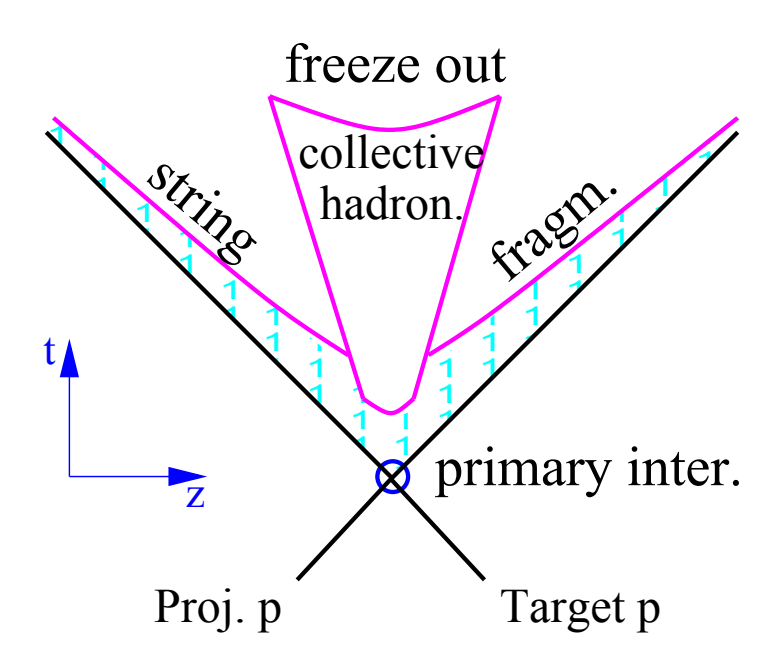


Figure 3.2: This is the schematic depiction of the space-time evolution of particle production in hadronic interaction in EPOS 1.99 or EPOS LHC [36]

### New features in EPOS LHC

The number of secondary particles produced by the clusters is a consequence of rescaling due to collective flows (particularly the radial flow). This property becomes relevant in the case of heavy-ion collisions where less number of particles are observed than generated by the model with any final state interaction [36]. Certainly, the proper hydrodynamic treatment (like in EPOS 2 and EPOS 3) requires a high multiplicity in the initial state so that after a long enough evolution of the core's large volume, it can finally give the correct multiplicity. It is referred to as the nuclear AA flow, which is characterized by the  $y_{rad}^{AA}$  (maximal radial rapidity) [36]. Using EPOS 2 or EPOS 3 with a more practical treatment involving hydrodynamical evolution with appropriate hadronization to deal with smaller systems such as pp, such effect was not observed [39]–[41]. Here, due to the rapid expansion of an extremely small volume of core, the large flow originates [36]. As a consequence, in the scenario of a highly dense system in a compact volume (where the critical energy density is achieved as a

consequence of multiple scatterings among partons in a pair of nucleons like pp) a distinct type of radial flow is introduced in the EPOS LHC. The cluster mass M remains unchanged before hadronization (multiplicity is conserved) for this pp flow, characterized by the  $y_{rad}^{pp}$  (maximal radial rapidity) but by the rescaling of total momentum  $P(\text{smaller }p_z \text{ compensates larger }p_T)$  after the radial boost, energy conservation is imposed. In a study on identified particle spectra from CMS [42], it has been observed that  $\langle p_T \rangle$  as a function of multiplicity is independent of the available center-of-mass energy but with an increase in multiplicity it increases. As this effect is directly linked to the intensity of radial flow [41], it becomes natural to parameterize all the flows as a function of  $M_{core}$  (total mass) which is directly related to the final multiplicity [36].

For the longitudinal flow

$$y_{long} = y_{long}^{mx} \cdot \log(\exp(\frac{y_{long}^{mi}}{y_{max}^{mx}}) + \frac{M_{core}}{M_{min}})$$
(3.2)

also the radial AA flow is

$$y_{rad}^{AA} = y_{rad}^{mx} \cdot \log(\frac{M_{core}}{M_{min}}) \tag{3.3}$$

and the radial pp flow becomes

$$y_{rad}^{pp} = y_{rad}^{px} \cdot \log(\frac{M_{core}}{M_{min}})$$
(3.4)

where the  $y_{rad}^{mx}$  parameter fixes the multiplicity and radial flow in HI and in pp the  $y_{rad}^{px}$  determine the evolution of  $\langle p_T \rangle$  as a function of multiplicity [36]. Since the longitudinal flow is the weakest, the parameters  $y_{long}^{mx}$  and  $y_{long}^{mi}$  are used for the fine tuning of multiplicity in  $pp(y_{long}^{mi})$  as well as in the case of HI interactions( $y_{long}^{mx}$ ).

Using the EPOS-LHC model we have generated data for pp collisions at  $\sqrt{s}$  =13 TeV and to ensure the quality of this generated data, we have compared its  $p_T$  spectra (charged particle) Fig.(3.3) and  $\eta$  distribution (charged particle) Fig.(3.4) with the available ALICE data. The ratio of

ALICE data and the simulated data is shown in the lower panel of the mentioned figures and it can be seen that the generated data agrees well with the ALICE data.

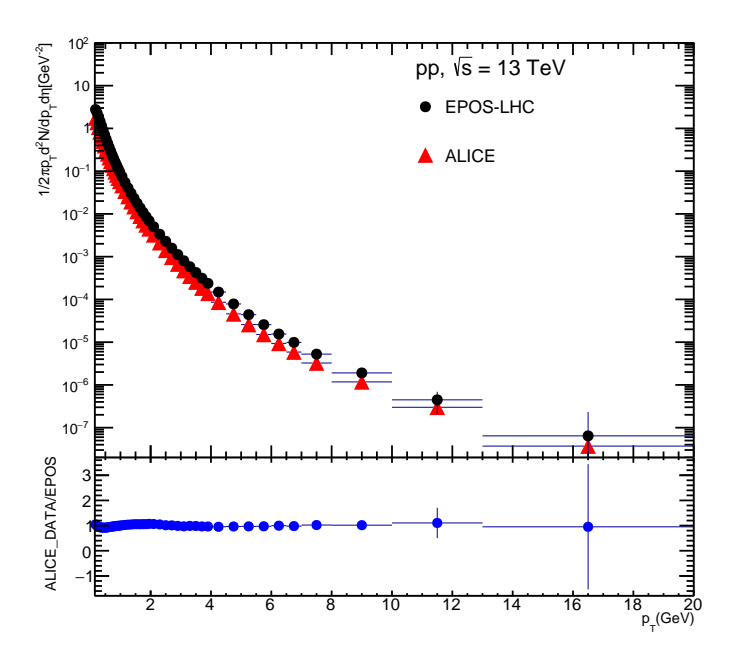


Figure 3.3: charged particle  $p_T$  spectra in  $p_T$  collisions at  $\sqrt{s} = 13$  TeV using EPOS-LHC is compared with experimental data from ALICE. The lower panel shows the ratio of both, indicating a nice agreement.

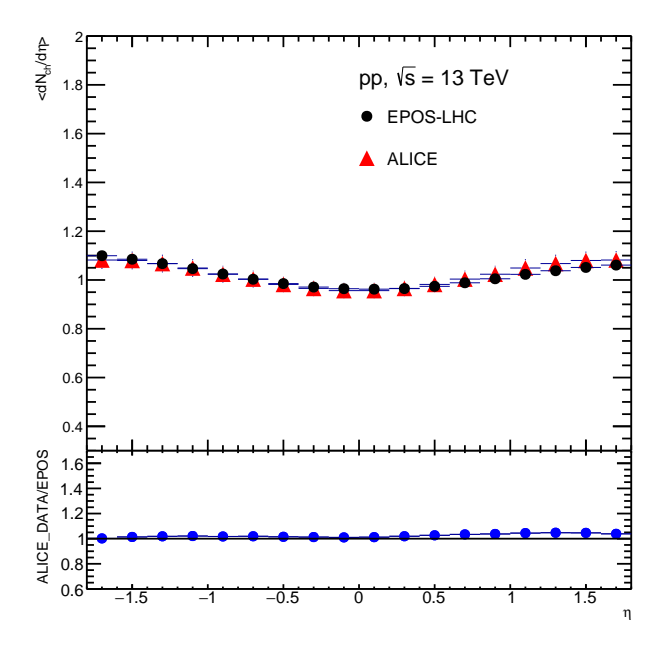


Figure 3.4: charged particle  $\eta$  distribution in pp collisions at  $\sqrt{s}=13$  TeV using EPOS-LHC is compared with experimental data from ALICE. The lower panel shows the ratio of both, indicating a nice agreement.

# 3.2 Spherocity: A tool to categorize event geometry

Spherocity is constructed to categorize the event geometry and it is conclusive from a previous event shape engineering analysis study [19] that for a better selection of events, spherocity along with  $N_{ch}$  must be preferred. In the same study, it has been discussed that there is a significant difference between the thermodynamics of events with different event topologies. One of the obvious conclusions of this study was that the isotropic events had a lower q as compared to jetty events, which means that they were tending more towards equilibrium. So it becomes essential for us to implement spherocity classification in our study too.

For an event, the transverse spherocity is defined as

$$S_0 = \frac{\pi^2}{4} \left( \frac{\sum_i |\vec{p}_{T_i} \times \hat{n}|}{\sum_i p_{T_i}} \right)^2$$
 (3.5)

Here, the unit vector  $\hat{n}(n_T, 0)$  is chosen such that it minimizes the Eq.3.5. It must be noted that the  $\hat{n}(n_T, 0)$  is that particular unit vector which is near to the majority of high  $p_T$  vectors, therefore, it does not necessarily always be in the region (in transverse plane) where the number of  $p_T$  vectors is large.

Spherocity is infrared and collinear safe [43] since it is confined to the transverse plane. Values of spherocity are related to event configuration in the transverse plane. Its extreme values are 0 and 1, where the 0 value corresponds to pencil-like events and 1 corresponds to isotropic events.

$$S = \frac{\pi^2}{4} \left( \frac{\int_0^{\pi} |p_T \sin \theta d\theta|}{\int_0^{\pi} p_T d\theta} \right)^2 = 1$$

It is expected that high multiplicity pp collisions must be dominated by isotropic events and low multiplicity are jetty dominated.

In this study, the spherocity distributions are taken in the pseudora-

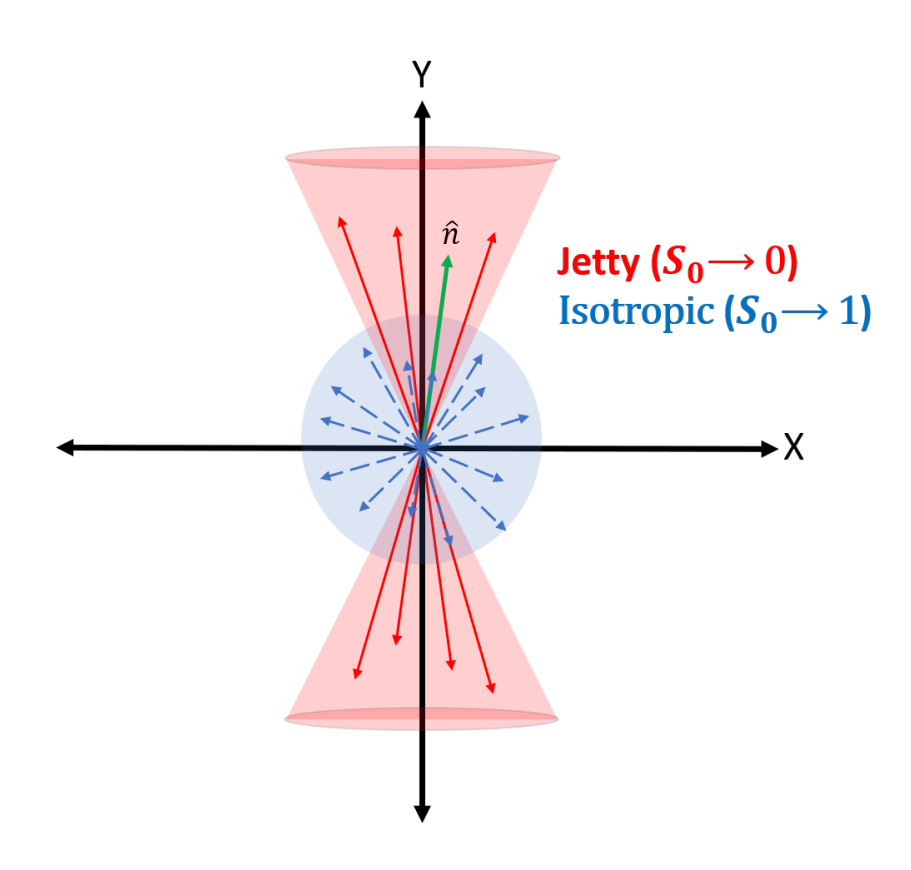


Figure 3.5: Figure showing jetty and isotropic events in the transverse plane. Figure taken from [44].

pidity range of  $|\eta|=0.8$  with a constraint of at least  $N_{ch}=5$  with  $p_T>0.15$  GeV/C. The disentanglement of the jetty and isotropic events from the  $S_0$  integrated events is done by implementing spherocity cuts on the simulated events (shown in Appendix A). Also, to mimic the experimental conditions  $N_{ch}$  have been chosen in the acceptance of ALICE's V0 detector with a psuedorapidity range of V0A (2.8 <  $\eta$  < 5.1) and V0C ( $-3.7 < \eta < -1.7$ ) [45]. The number of  $N_{ch}$  in an event in various V0 multiplicity classes is mentioned in Table 3.1.

V0M class	I	II	III	IV	V	VI	VII	VIII	IX	X
$N_{ch}$	50-140	42-49	36-41	31-35	27-30	23-26	19-22	15-18	10-14	0-9

Table 3.1: V0M classes and their corresponding multiplicities (charged particles)

In our study, we have iterated over the whole transverse plane (360°) with a precision of  $0.1^{\circ}$  to find out the correct  $\hat{n}$  and used that to calculate the spherocity for each event.

Also, for the classification of the jetty and isotropic events, we have im-

plemented cuts on the spherocity distribution at the top 20 % and bottom 20 % events for isotropic and jetty events respectively (shown in Appendix A). The cuts are obtained to be  $S_0 = 0.35252$  for jetty and  $S_0 = 0.69925$  for isotropic events.

To ensure the quality of simulated data, we have plotted the spherocity distribution for different multiplicity classes Fig.(3.6). As expected, it is found that the high multiplicity pp collisions are dominated by isotropic events whereas jetty events dominate the low multiplicity collisions.

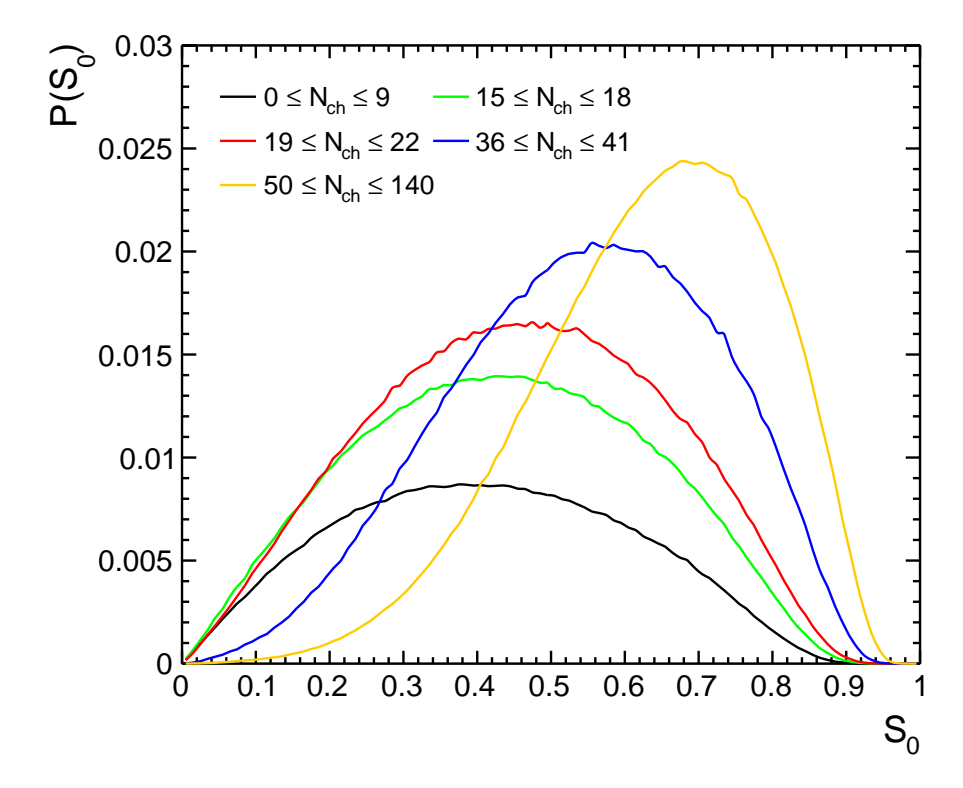


Figure 3.6: Spherocity distribution for the mentioned multiplicity classes. pp collisions at  $\sqrt{s}=13$  TeV using EPOS-LHC

#### 3.3 Tsallis statistics

As the Boltzmann-Gibbs function only describes the  $p_T$  spectra up to a certain low value of  $p_T$ , so a generalisation is done for this function, namely the Tsallis function. Its low- $p_T$  exponential and high- $p_T$  power-law behaviour gives a complete spectral description of identified secondaries produced in pp collisions. This function gives a much better description of the systems which have not attained equilibrium yet [44]. There are various different versions of Tsallis distribution among which we have used a thermodynamically consistent Tsallis nonextensive distribution shown in [46]. The particle distribution at midrapidity is given in the tsallis formalism by,

$$\frac{1}{p_T} \frac{d^2 N}{dp_T dy} = \frac{gV m_T}{(2\pi)^2} \left[ 1 + (q-1) \frac{m_T}{T} \right]^{-q/(q-1)}$$
(3.6)

where V is the volume parameter, g is the degeneracy factor,  $m_T = \sqrt{p_T^2 + m^2}$  is the transverse mass and q is the non-extensive parameter which gives the extend of non-equilibrium. Tsallis distribution reduces to Boltzmann-Gibbs distribution in the limit of  $q \longrightarrow 1$ . This function is widely used to describe particle spectra in high-energy hadronic and heavy-ion collisions [47]–[49].

In this study, we have implemented the above-mentioned Tsallis function to describe the multiplicity-wise  $p_T$  spectra of pions and kaons for all three event geometries. By fitting Tsallis function the T, q and R parameters are obtained for each multiplicity and spherocity class. In the later sections we have discussed the physical significance of the obtained values of these parameters and have used these parameters to obtain the common freeze-out temperature and the strength of average radial flow by using the formalism introduced in [18].

# Chapter 4

## Results and Discussions

In this chapter, the results of our study are presented and discussed. In Fig.(4.1) the Tsallis fitted multiplicity wise  $p_T$  spectra of kaons and pions for isotropic, spherocity integrated and jetty cases are shown. In these figures, the lower panel shows the ratio of the fit values with respect to the simulated value.

In Fig.(4.2) the Tsallis extracted temperature parameter and q (non-extensive parameter) are shown. Later we used these extracted parameters to calculate the isothermal compressibility. For each particle, these parameters are obtained for each spherocity class. The Tsallis volume parameter is also extracted and shown in Fig.(4.3). It is briefly discussed below that this so-called "volume parameter" is actually not related to the size of the system [50].

In Fig.(4.4) we have shown the linear fit using the formalism introduced in [18] to obtain the freeze-out temperature and strength of radial flow. A few assumptions and features of the mentioned formalism are also discussed below.

The obtained spherocity-class-wise freeze-out temperature and  $\langle u_t \rangle$  are shown in Fig.(4.5). The difference in values of freeze-out temperature for each spherocity class is also discussed below. Then the obtained common freeze-out temperature is used to calculate the  $k_T$  which is shown for each spherocity class in Fig.(4.6).

### 4.1 Tsallis fit for the obtained $p_T$ spectra

The multiplicity-wise  $p_T$  spectra are obtained for pions and hadrons using the EPOS-LHC model, the multiplicity classes are mentioned in Table.(3.1). For this study, we have first implemented the spherocity classification and then the multiplicity classes on the  $p_T$  spectra for both pions and kaons.

The Tsallis function Eq.(3.6) is then used to fit multiplicity-wise  $p_T$  spectra to obtain the information of T, q and R parameters. Since one of the purposes of this study is to study the system using hydrodynamics so we have fitted the Tsallis function under the hydrodynamic limit. The purpose of this is to see the variation of T, q and R parameters with respect to the charged particle multiplicity i.e. the information of non-equilibrium and thermalization based on multiplicity.

The fitting is also done separately for all three spherocity classes, thus it will help us to establish the difference in thermalization and non-equilibrium among the isotropic and jetty events, this discussed distinction is discussed in the next sections.

Fig.(4.1) shows the multiplicity-wise Tsallis fitted  $p_T$  of pions and kaon for each spheroctiy class, namely isotropic, spherocity integrated and jetty. In the lower panel, the ratio of obtained fit value and simulated value (from the EPOS-LHC generated data) is shown and it can be seen that all the fits reasonably agree with the simulated data.

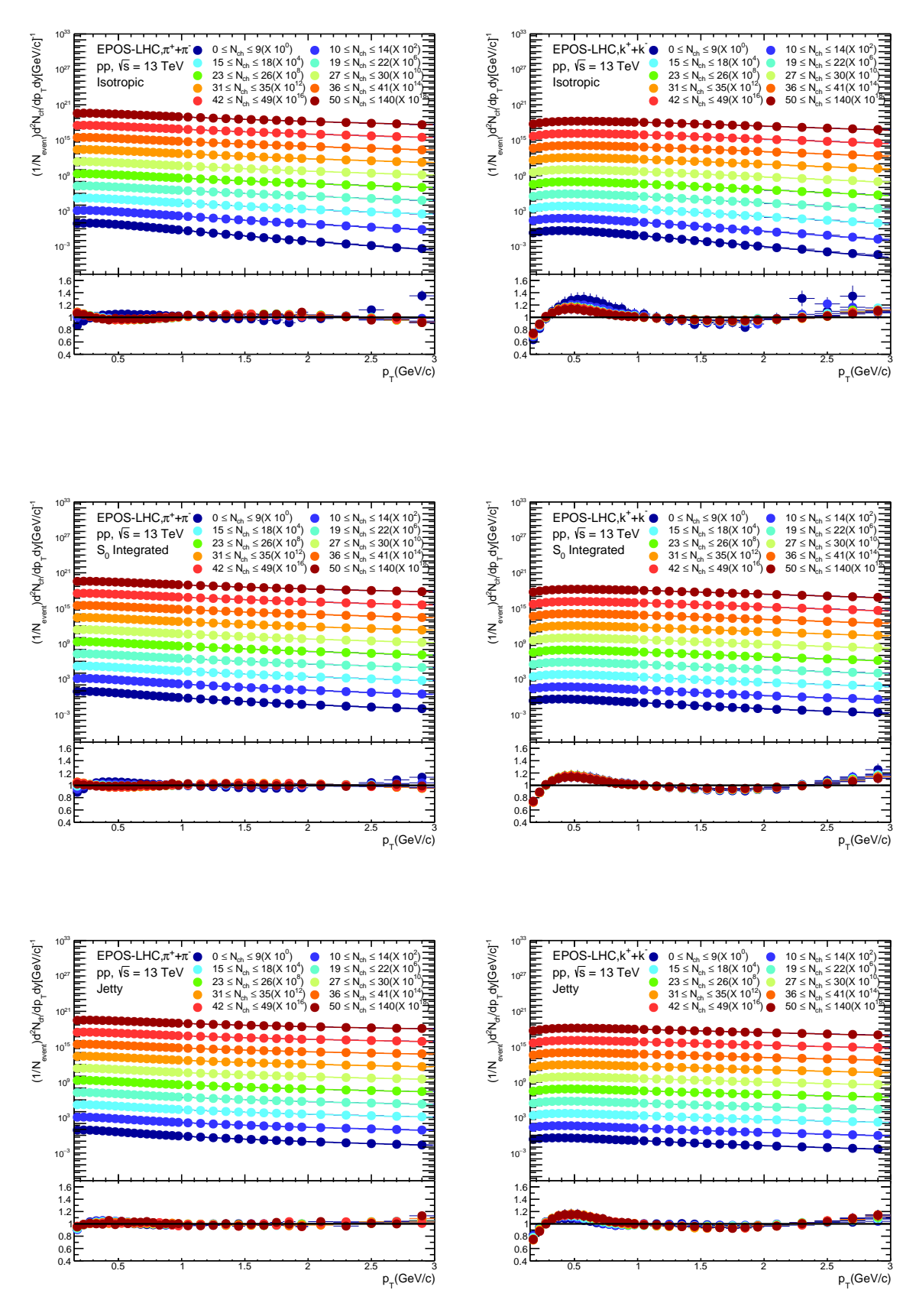


Figure 4.1: Fitting of multiplicity-wise  $p_T$  spectra of pions and kaon for all three spherocity classes

## 4.2 Extracted T, q and R parameters

Using the EPOS-LHC generated data, the fits are performed to obtain the T, q and R parameters using the Tsallis function for different spherocity and multiplicity classes. The results are shown in Fig.(4.2) and it can be seen that the temperature parameter is higher for isotropic events as compared to the case of jetty events while the q parameter shows an opposite trend. The values of q are shown to be lowest for isotropic events and maximum for jetty events, which means that jetty events are further from equilibrium as compared to isotropic events.

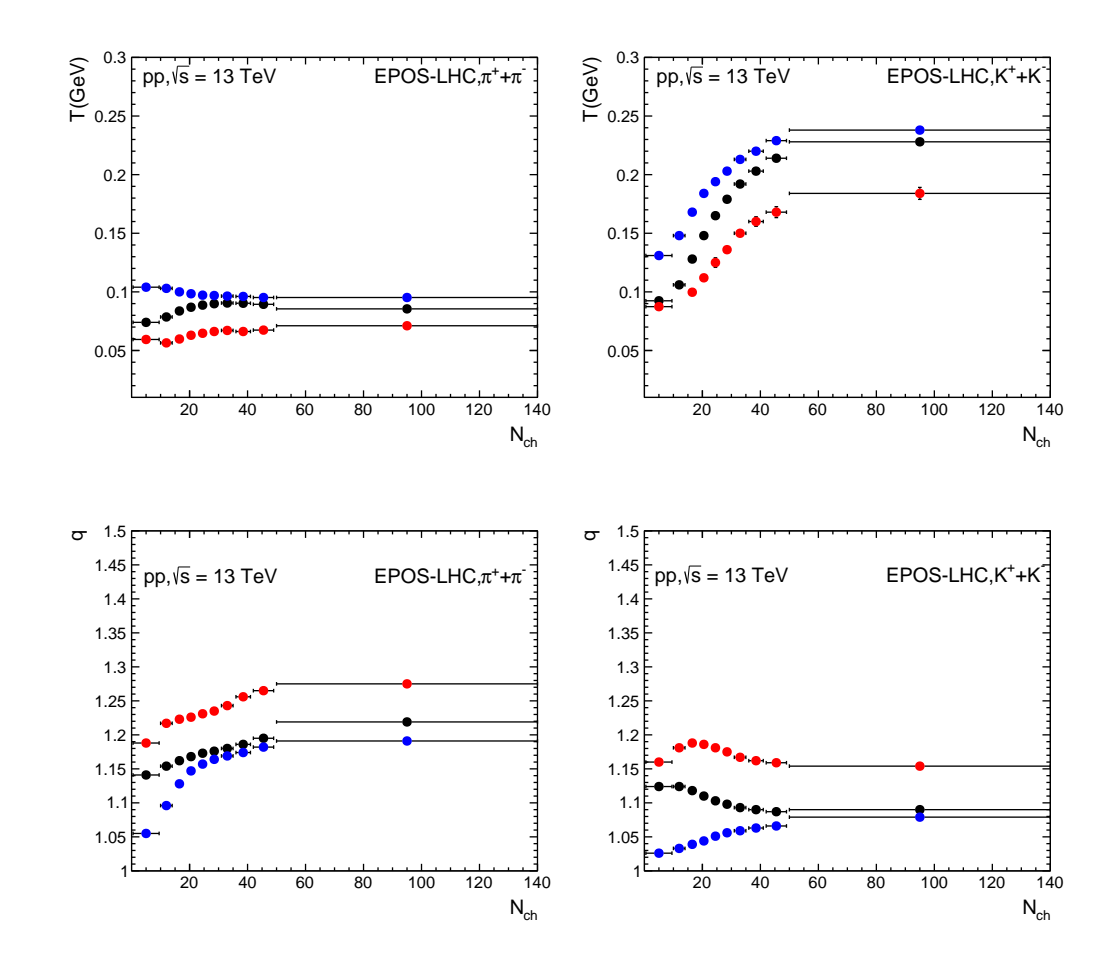


Figure 4.2: T for identified particles are shown here from EPOS-LHC data for Spherocity integrated, isotropic and jetty events

- $(\bullet)$   $S_0$  integrated
- (•) Isotropic
- (•) Jetty

In Fig.(4.3) R parameter is extracted from the Tsallis function and it

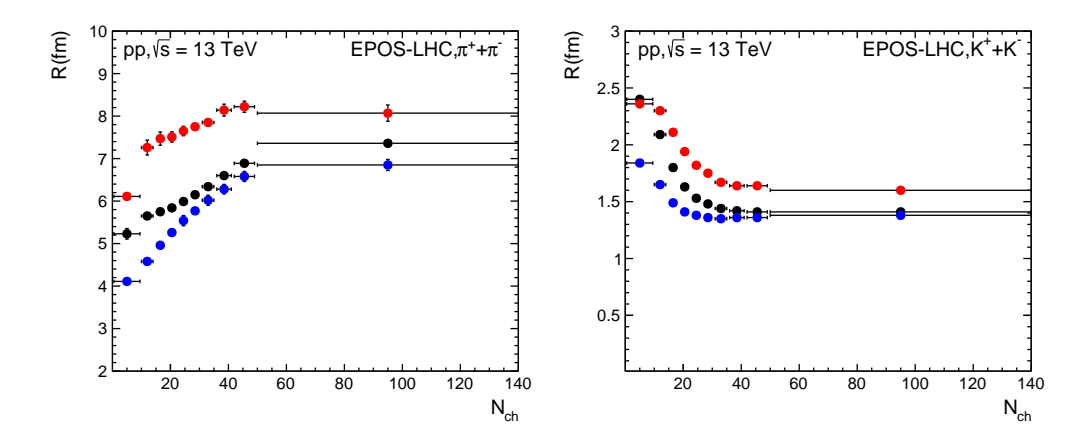


Figure 4.3: R for pion and kaon are shown here from EPOS-LHC data for Spherocity integrated, isotropic and jetty events

- (•)  $S_0$  integrated
- (•) Isotropic
- (•) Jetty

is shown as a function of  $N_{ch}$  for different event shape classes. It must be noted that this radius parameter, R, is not necessarily related to the size of the system, from the HBT experimental analysis, it is determined that this R parameter is actually related to the normalisation in distribution function which explains the particle spectra [50].

# 4.3 Kinetic freeze-out temperature and radial flow strength

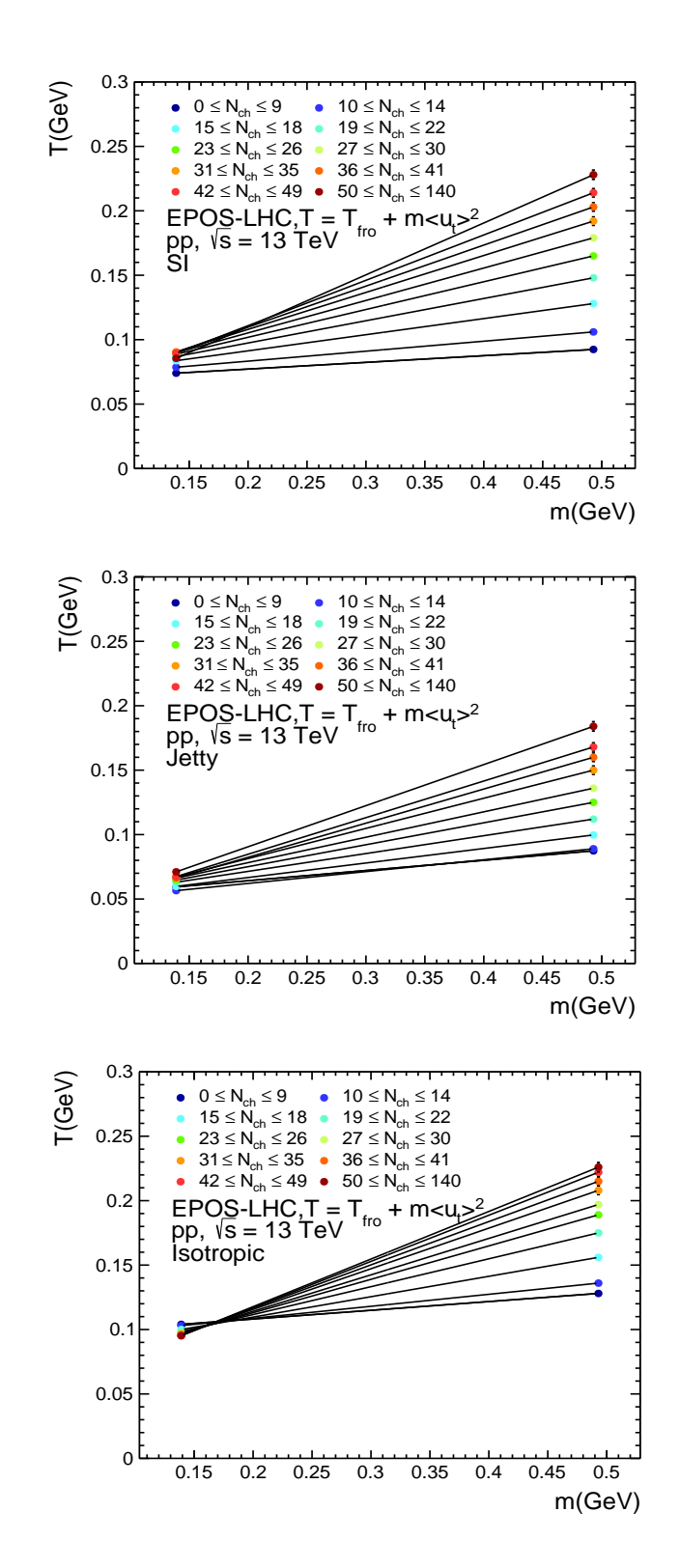


Figure 4.4: Fitting is done using Eq.(4.1) to extract  $T_{fro}$  and  $\langle u_t \rangle$ 

The temperature parameter which is obtained from Tsallis fitting is hadron mass dependent [51]. This is usually interpreted as the presence of a radial flow in the system, which produces an increment in the  $p_T$  of hadrons proportional to their respective masses. This ultimately results in a different value of the temperature instead of the original freeze-out temperature which is same for all hadrons [18], [52], [53]. In our study we have used the formalism introduced in [18]. In this formalism the radial flow is explained as

$$T = T_{fro} + m \left\langle u_t \right\rangle^2 \tag{4.1}$$

where  $T_{fro}$  refers to the freeze-out temperature and  $\langle u_t \rangle$  corresponds to the strength of average radial flow. It is the innate assumption of this formalism that different particle species freeze-out at a common temperature. As shown in Fig.(4.4), we have used this formalism along with the event shape categorization to extract the freeze-out temperature and  $\langle u_t \rangle$ .

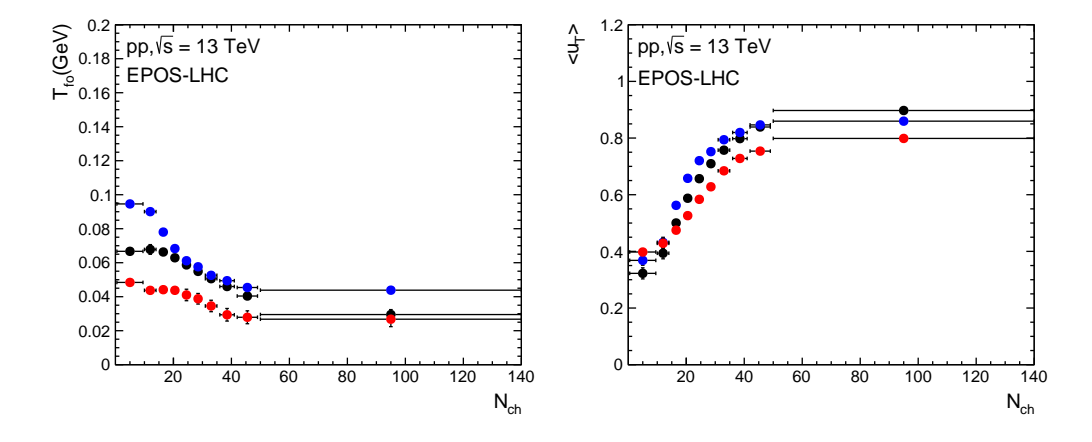


Figure 4.5:  $T_{fro}$  and  $\langle u_t \rangle$  are extracted using Eq.(4.1) from the EPOS-LHC generated data and are shown in this figure for all three event topologies.

- $(\bullet)$   $S_0$  integrated
- (•) Isotropic
- (•) Jetty

It is observed that  $T_{fro}$  decreases with  $N_{ch}$  and shows the maximum value for isotropic events and the minimum for jetty events. For all the spherocity classes, the  $T_{fo}$  is found to be decreasing with an increase in multiplicity, this can be explained by the fact that flow is higher in events

with high multiplicity as compared to low multiplicity events, therefore, the higher the multiplicity the more the time system takes to freeze-out which results in lower freeze-out temperature.

It is also found out that the maximum strength of average radial flow is observed for isotropic events whereas it is minimum for jetty events, it is also observed that  $\langle u_t \rangle$  shows an increasing trend with  $N_{ch}$  as shown in Fig.(4.5).

This extracted  $T_{fro}$  along with q values for different different spherocity classes can be used to calculate  $k_T$  for pions and kaons. The extracted  $k_T$  profile for pions and hadrons is shown in Fig.(4.6).

### 4.4 Results: Dissipative properties

#### 4.4.1 Spherocity-wise $k_T$ profile for pions and kaons

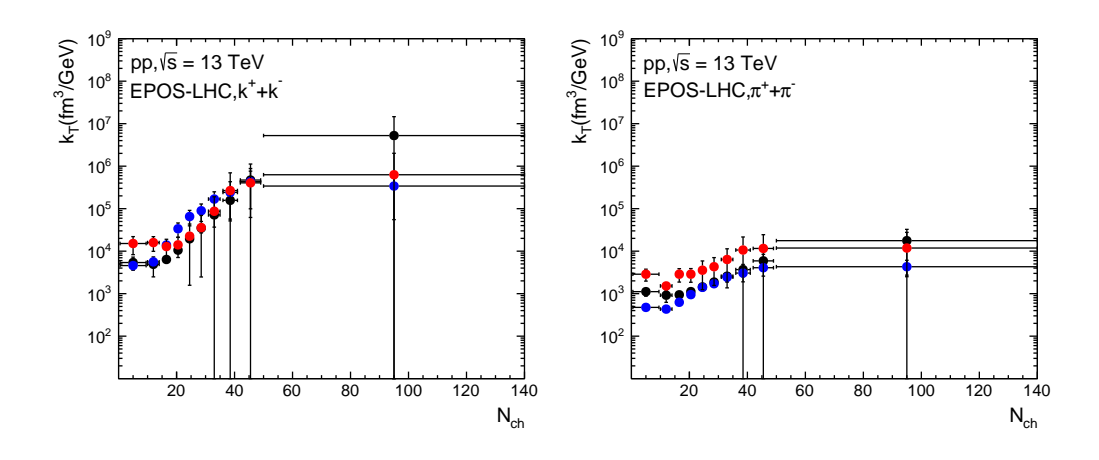


Figure 4.6:  $k_T$  for identified particles are shown here from EPOS-LHC data for Spherocity integrated, isotropic and jetty events

- $(\bullet)$   $S_0$  integrated
- (•) Isotropic
- (•) Jetty

We have used the common freeze-out temperature (without the radial flow component) for the purpose of calculating the isothermal compressibility for each spherocity class. The obtained values of  $k_T$  are shown in the above Fig.(4.6). It is evident from these results that there is an increase in  $k_T$  with an increase in charged particle multiplicity and this trend of  $k_T$  is a direct consequence of the fact that the  $T_{fo}$  is found to be decreasing with an increase in charged particle multiplicity.

#### 4.4.2 Spherocity-wise $\eta/s$ profile for pions and kaons

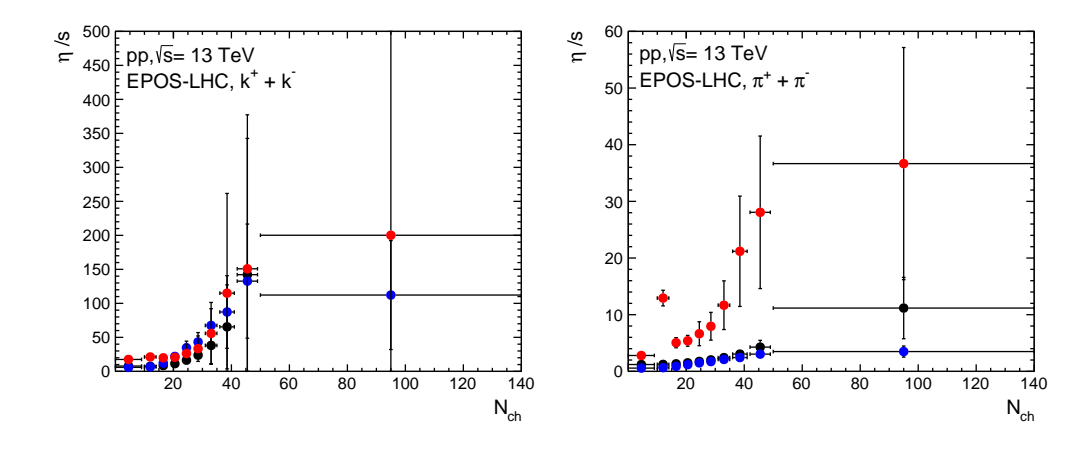


Figure 4.7:  $\eta/s$  for identified particles are shown here from EPOS-LHC data for Spherocity integrated, isotropic and jetty events

- ( $\bullet$ )  $S_0$  integrated
- (•) Isotropic
- (•) Jetty

Here we have used the common freeze-out temperature (without radial flow component) for calculating the  $\eta/s$  for each spherocity class. For both kaons and pions it is observed that  $\eta/s$  increase with multiplicity and for jetty events  $\eta/s$  remains higher as compared to isotropic events. The increasing trend of  $\eta/s$  is the direct result of the decreasing nature of  $T_{fo}$  (common freeze-out temperature) with respect to  $N_{ch}$ . The obtained values of  $\eta/s$  are shown in the above Fig.(4.7).

## Chapter 5

# **Summary and Conclusion**

In this study, we have analysed pp collisions at  $\sqrt{s} = 13$  TeV using a hydrodynamics-inspired (EPOS-LHC) model. We have also implemented spherocity classification to disentangle isotropic events from the jetty ones. T, q, and R parameters were extracted by Tsallis fitting on generated  $p_T$  spectra for pions and kaons for all spherocity classes. Later we used the values of these obtained parameters to calculate the common freeze-out temperature and strength of average radial flow for all three spherocity classes. The obtained freeze-out temperature along with the q input was then used to calculate  $k_T$  and  $\eta/s$  for both kaons and pions.

The results obtained for the discussed parameters and quantities are mentioned below:

- 1. For both kaons and pions the Tsallis extracted temperature parameter is found to be more for isotropic events as compared to jetty events.
- 2. The Tsallis extracted non-extensive parameter is found to be less for isotropic events as compared to jetty events for both pions and kaon.
- 3. For both kaons and pions the Tsallis extracted R parameter is found to be minimum for isotopic events as compared to jetty events. Also the trend of R parameter with respect to  $N_{ch}$  for all spherocity classes is decreasing for kaons while for the pions it follows an increasing trend.

- 4. The common freeze-out temperature  $(T_{fo})$  is found to be decreasing with respect to  $N_{ch}$  for all spherocity classes. This occurs because higher multiplicity systems take longer to freeze-out as compared to low multiplicity systems.
- 5. The  $T_{fo}$  is found to be more for isotropic events as compared to jetty events.
- 6. For all the spherocity classes the strength of average radial flow  $(\langle u_t \rangle)$  is found to increase with respect to  $N_{ch}$ .
- 7. It is found that for all the spherocity classes the isothermal compressibility and shear viscosity are found to be increasing with an increase in multiplicity, this can be explained by the decreasing kinetic freezeout temperature with an increase in multiplicity.

# Appendix A

## A.1 Spherocity cuts

To classify the jetty events and isotropic events, we have implemented cuts on the spherocity distribution. The cuts are taken at the top 20 % (isotropic) and bottom 20 % (jetty) of the spherocity distribution. The cuts values are obtained to be 0.35525 and 0.69252 for jetty and isotropic events respectively.

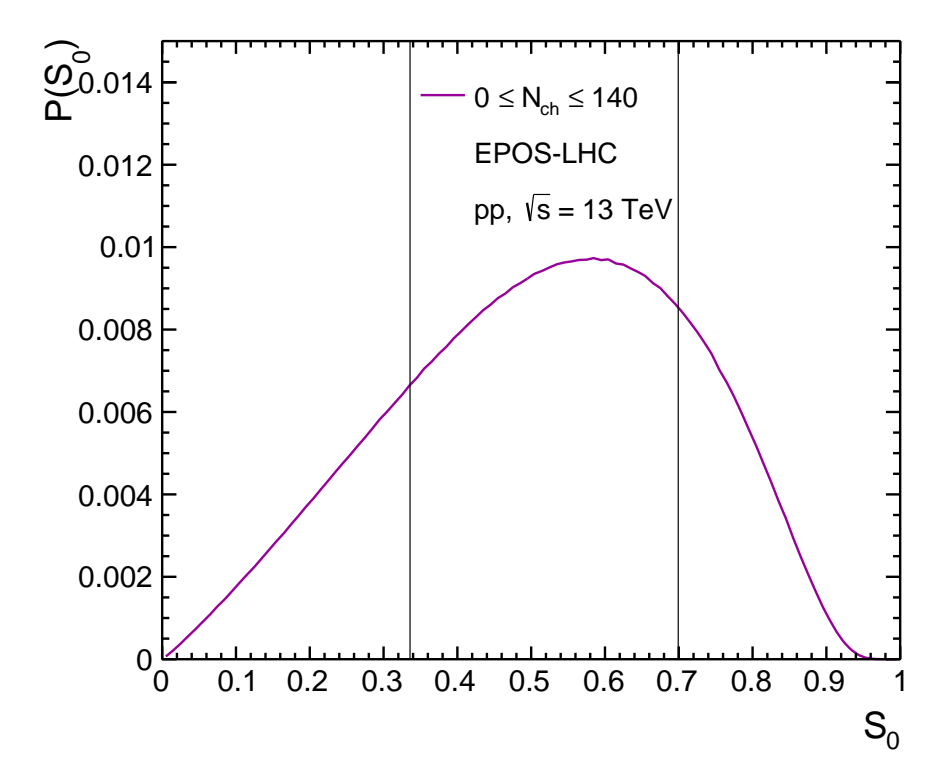
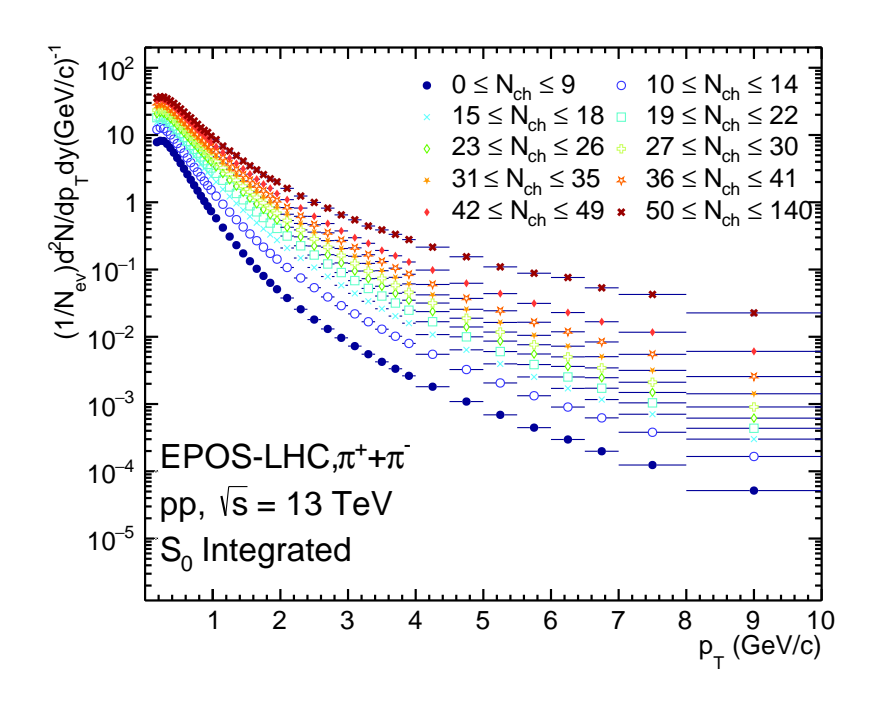


Figure A.1: Cuts on spherocity are implemented for the classification of jetty and isotropic events

## A.2 Unscaled $p_T$ spectra of pions and kaons



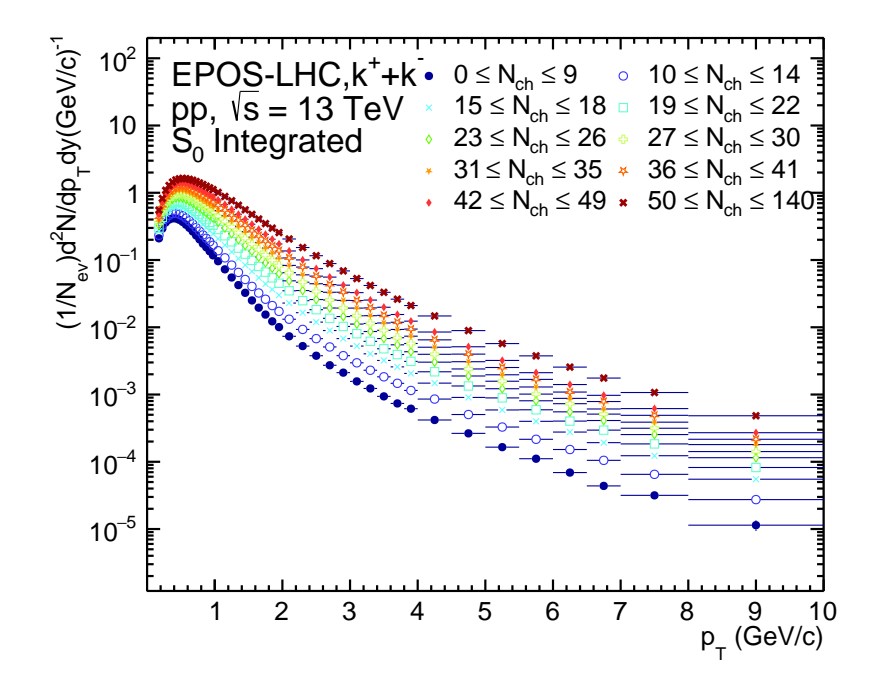


Figure A.2:  $p_T$ -spectra of pions and kaons from EPOS-LHC for pp at  $\sqrt{s}=13$  TeV for  $S_0$  integrated events

# Bibliography

- [1] C. Shen and U. Heinz, "The road to precision: Extraction of the specific shear viscosity of the quark-gluon plasma," *Nucl. Phys. News*, vol. 25, no. 2, pp. 6–11, 2015. DOI: 10.1080/10619127.2015. 1006502. arXiv: 1507.01558 [nucl-th].
- [2] W. Greiner, S. Schramm, and E. Stein, *Quantum chromodynamics*. 2002.
- [3] R. Sahoo, "Possible Formation of QGP-droplets in Proton-Proton Collisions at the CERN Large Hadron Collider," *AAPPS Bull.*, vol. 29, no. 4, pp. 16–21, 2019. DOI: 10.22661/AAPPSBL.2019.29.4.16. arXiv: 1908.10566 [nucl-ex].
- [4] B. Mohanty, "Exploring the QCD phase diagram through high energy nuclear collisions: An overview," *PoS*, vol. CPOD2013, p. 001, 2013. DOI: 10.22323/1.185.0001. arXiv: 1308.3328 [nucl-ex].
- [5] S. A. Bass et al., "Last call for RHIC predictions," Nucl. Phys. A, vol. 661, L. Riccati, M. Masera, and E. Vercellin, Eds., pp. 205–260, 1999. DOI: 10.1016/S0375-9474(99)85024-6. arXiv: nucl-th/9907090.
- [6] F. Antinori et al., "Production of strange and multistrange hadrons in nucleus nucleus collisions at the SPS," Nucl. Phys. A, vol. 661, L. Riccati, M. Masera, and E. Vercellin, Eds., pp. 130–139, 1999. DOI: 10.1016/S0375-9474(99)85015-5.
- [7] B. B. Abelev *et al.*, "Multi-strange baryon production at mid-rapidity in Pb-Pb collisions at  $\sqrt{s_{NN}} = 2.76$  TeV," *Phys. Lett. B*, vol. 728,

- pp. 216–227, 2014, [Erratum: Phys.Lett.B 734, 409–410 (2014)]. DOI: 10.1016/j.physletb.2014.05.052. arXiv: 1307.5543 [nucl-ex].
- [8] J. Adams *et al.*, "Experimental and theoretical challenges in the search for the quark gluon plasma: The STAR Collaboration's critical assessment of the evidence from RHIC collisions," *Nucl. Phys. A*, vol. 757, pp. 102–183, 2005. DOI: 10.1016/j.nuclphysa.2005.03. 085. arXiv: nucl-ex/0501009.
- [9] M. L. Miller, K. Reygers, S. J. Sanders, and P. Steinberg, "Glauber modeling in high energy nuclear collisions," Ann. Rev. Nucl. Part. Sci., vol. 57, pp. 205–243, 2007. DOI: 10.1146/annurev.nucl.57.090506.123020. arXiv: nucl-ex/0701025.
- [10] B. B. Abelev *et al.*, "Centrality, rapidity and transverse momentum dependence of  $J/\psi$  suppression in Pb-Pb collisions at  $\sqrt{s_{\rm NN}}$ =2.76 TeV," *Phys. Lett. B*, vol. 734, pp. 314–327, 2014. DOI: 10.1016/j. physletb.2014.05.064. arXiv: 1311.0214 [nucl-ex].
- [11] J. Adam *et al.*, "J/ $\psi$  suppression at forward rapidity in Pb-Pb collisions at  $\sqrt{s_{\rm NN}}=5.02$  TeV," *Phys. Lett. B*, vol. 766, pp. 212–224, 2017. DOI: 10.1016/j.physletb.2016.12.064. arXiv: 1606.08197 [nucl-ex].
- [12] T. Matsui and H. Satz, " $J/\psi$  Suppression by Quark-Gluon Plasma Formation," *Phys. Lett. B*, vol. 178, pp. 416–422, 1986. DOI: 10 . 1016/0370-2693(86)91404-8.
- [13] J. Adam *et al.*, "Enhanced production of multi-strange hadrons in high-multiplicity proton-proton collisions," *Nature Phys.*, vol. 13, pp. 535–539, 2017. DOI: 10.1038/nphys4111. arXiv: 1606.07424 [nucl-ex].
- [14] B. Alver et al., "System size dependence of cluster properties from two-particle angular correlations in Cu+Cu and Au+Au collisions at s(NN)\*\*(1/2) = 200-GeV," Phys. Rev. C, vol. 81, p. 024904, 2010. DOI: 10.1103/PhysRevC.81.024904. arXiv: 0812.1172 [nucl-ex].

- [15] S. Borsanyi, Z. Fodor, C. Hoelbling, S. D. Katz, S. Krieg, and K. K. Szabo, "Full result for the QCD equation of state with 2+1 flavors," *Phys. Lett. B*, vol. 730, pp. 99–104, 2014. DOI: 10.1016/j.physletb. 2014.01.007. arXiv: 1309.5258 [hep-lat].
- [16] V. Khachatryan *et al.*, "Evidence for collectivity in pp collisions at the LHC," *Phys. Lett. B*, vol. 765, pp. 193–220, 2017. DOI: 10.1016/j.physletb.2016.12.009. arXiv: 1606.06198 [nucl-ex].
- [17] G. Aad et al., "Observation of Long-Range Elliptic Azimuthal Anisotropies in  $\sqrt{s}$  =13 and 2.76 TeV pp Collisions with the ATLAS Detector," Phys. Rev. Lett., vol. 116, no. 17, p. 172 301, 2016. DOI: 10.1103/PhysRevLett.116.172301. arXiv: 1509.04776 [hep-ex].
- [18] A. Adare *et al.*, "Identified charged hadron production in p+p collisions at  $\sqrt{s}=200$  and 62.4 GeV," *Phys. Rev. C*, vol. 83, p. 064903, 2011. DOI: 10 . 1103 / PhysRevC . 83 . 064903. arXiv: 1102 . 0753 [nucl-ex].
- [19] A. Khuntia, S. Tripathy, A. Bisht, and R. Sahoo, "Event shape engineering and multiplicity dependent study of identified particle production in proton + proton collisions at √s = 13 TeV using PYTHIA8," J. Phys. G, vol. 48, no. 3, p. 035102, 2021. DOI: 10.1088/1361-6471/abb1f8. arXiv: 1811.04213 [hep-ph].
- [20] P. Romatschke and U. Romatschke, "Viscosity Information from Relativistic Nuclear Collisions: How Perfect is the Fluid Observed at RHIC?" Phys. Rev. Lett., vol. 99, p. 172301, 2007. DOI: 10.1103/PhysRevLett.99.172301. arXiv: 0706.1522 [nucl-th].
- [21] T. Hirano and M. Gyulassy, "Perfect fluidity of the quark gluon plasma core as seen through its dissipative hadronic corona," *Nucl. Phys. A*, vol. 769, pp. 71–94, 2006. DOI: 10.1016/j.nuclphysa. 2006.02.005. arXiv: nucl-th/0506049.
- [22] M. Mukherjee, S. Basu, A. Chatterjee, et al., "Isothermal compressibility of hadronic matter formed in relativistic nuclear collisions,"

- Phys. Lett. B, vol. 784, pp. 1-5, 2018. DOI: 10.1016/j.physletb.
  2018.07.021. arXiv: 1708.08692 [nucl-ex].
- [23] D. Sahu, S. Tripathy, R. Sahoo, and S. K. Tiwari, "Possible formation of a perfect fluid in pp, p–Pb, Xe–Xe and Pb–Pb collisions at the Large Hadron Collider energies: a color string percolation approach," Eur. Phys. J. A, vol. 58, no. 4, p. 78, 2022. DOI: 10.1140/epja/s10050-022-00735-5. arXiv: 2001.01252 [hep-ph].
- [24] B. Mohanty and J.-e. Alam, "Velocity of sound in relativistic heavy ion collisions," *Phys. Rev. C*, vol. 68, p. 064903, 2003. DOI: 10.1103/PhysRevC.68.064903. arXiv: nucl-th/0301086.
- [25] G. P. Kadam and H. Mishra, "Dissipative properties of hot and dense hadronic matter in an excluded-volume hadron resonance gas model," *Phys. Rev. C*, vol. 92, no. 3, p. 035 203, 2015. DOI: 10.1103/PhysRevC.92.035203. arXiv: 1506.04613 [hep-ph].
- [26] J. R. Bezerra, R. Silva, and J. A. S. Lima, "Transport Coefficients and Nonextensive Statistics," *Physica A*, vol. 322, pp. 256–266, 2003.
   DOI: 10.1016/S0378-4371(02)01813-7. arXiv: cond-mat/0201541.
- [27] S. Gavin, "TRANSPORT COEFFICIENTS IN ULTRARELATIVIS-TIC HEAVY ION COLLISIONS," Nucl. Phys. A, vol. 435, pp. 826–843, 1985. DOI: 10.1016/0375-9474(85)90190-3.
- [28] J. Cleymans and D. Worku, "Relativistic Thermodynamics: Transverse Momentum Distributions in High-Energy Physics," Eur. Phys. J. A, vol. 48, p. 160, 2012. DOI: 10.1140/epja/i2012-12160-0. arXiv: 1203.4343 [hep-ph].
- [29] S. K. Tiwari, S. Tripathy, R. Sahoo, and N. Kakati, "Dissipative Properties and Isothermal Compressibility of Hot and Dense Hadron Gas using Non-extensive Statistics," *Eur. Phys. J. C*, vol. 78, no. 11, p. 938, 2018. DOI: 10.1140/epjc/s10052-018-6411-y. arXiv: 1709.06352 [hep-ph].

- [30] O. Moroz, "Shear and bulk viscosities of the hadron gas within relaxation time approximation and its test," *Ukr. J. Phys.*, vol. 58, pp. 1127–1131, 2013. arXiv: 1312.6429 [hep-ph].
- [31] M. Cannoni, "Relativistic  $\langle \sigma v_{rel} \rangle$  in the calculation of relics abundances: a closer look," *Phys. Rev. D*, vol. 89, no. 10, p. 103533, 2014. DOI: 10.1103/PhysRevD.89.103533. arXiv: 1311.4494 [astro-ph.CO].
- [32] P. Gondolo and G. Gelmini, "Cosmic abundances of stable particles: Improved analysis," *Nucl. Phys. B*, vol. 360, pp. 145–179, 1991. DOI: 10.1016/0550-3213(91)90438-4.
- [33] A. Adare et al., "Charged hadron multiplicity fluctuations in Au+Au and Cu+Cu collisions from  $\sqrt{s_{NN}}=22.5$  to 200 GeV," Phys. Rev. C, vol. 78, p. 044 902, 2008. DOI: 10.1103/PhysRevC.78.044902. arXiv: 0805.1521 [nucl-ex].
- [34] S. Mrowczynski, "Hadronic matter compressibility from event by event analysis of heavy ion collisions," *Phys. Lett. B*, vol. 430, pp. 9–14, 1998. DOI: 10.1016/S0370-2693(98)00492-4. arXiv: nucl-th/9712030.
- [35] K. Werner, F.-M. Liu, and T. Pierog, "Parton ladder splitting and the rapidity dependence of transverse momentum spectra in deuterongold collisions at RHIC," *Phys. Rev. C*, vol. 74, p. 044902, 2006. DOI: 10.1103/PhysRevC.74.044902. arXiv: hep-ph/0506232.
- [36] T. Pierog, I. Karpenko, J. M. Katzy, E. Yatsenko, and K. Werner, "EPOS LHC: Test of collective hadronization with data measured at the CERN Large Hadron Collider," *Phys. Rev. C*, vol. 92, no. 3, p. 034 906, 2015. DOI: 10.1103/PhysRevC.92.034906. arXiv: 1306. 0121 [hep-ph].
- [37] K. Werner, I. Karpenko, T. Pierog, M. Bleicher, and K. Mikhailov, "Event-by-Event Simulation of the Three-Dimensional Hydrodynamic Evolution from Flux Tube Initial Conditions in Ultrarelativistic Heavy

- Ion Collisions," *Phys. Rev. C*, vol. 82, p. 044 904, 2010. DOI: 10.1103/ PhysRevC.82.044904. arXiv: 1004.0805 [nucl-th].
- [38] K. Werner, "Core-corona separation in ultra-relativistic heavy ion collisions," *Phys. Rev. Lett.*, vol. 98, p. 152 301, 2007. DOI: 10.1103/PhysRevLett.98.152301. arXiv: 0704.1270 [nucl-th].
- [39] K. Werner, B. Guiot, I. Karpenko, and T. Pierog, "Analysing radial flow features in p-Pb and p-p collisions at several TeV by studying identified particle production in EPOS3," *Phys. Rev. C*, vol. 89, no. 6, p. 064903, 2014. DOI: 10.1103/PhysRevC.89.064903. arXiv: 1312. 1233 [nucl-th].
- [40] K. Werner, M. Bleicher, B. Guiot, I. Karpenko, and T. Pierog, "Evidence for Flow from Hydrodynamic Simulations of p-Pb Collisions at 5.02 TeV from ν<sub>2</sub> Mass Splitting," Phys. Rev. Lett., vol. 112, no. 23, p. 232 301, 2014. DOI: 10.1103/PhysRevLett.112.232301. arXiv: 1307.4379 [nucl-th].
- [41] K. Werner, I. Karpenko, T. Pierog, M. Bleicher, and K. Mikhailov, "Evidence for hydrodynamic evolution in proton-proton scattering at 900 GeV," *Phys. Rev. C*, vol. 83, p. 044915, 2011. DOI: 10.1103/PhysRevC.83.044915. arXiv: 1010.0400 [nucl-th].
- [42] S. Chatrchyan et al., "Study of the Inclusive Production of Charged Pions, Kaons, and Protons in pp Collisions at  $\sqrt{s}=0.9$ , 2.76, and 7 TeV," Eur. Phys. J. C, vol. 72, p. 2164, 2012. DOI: 10.1140/epjc/s10052-012-2164-1. arXiv: 1207.4724 [hep-ex].
- [43] G. P. Salam, "Towards Jetography," Eur. Phys. J. C, vol. 67, pp. 637–686, 2010. DOI: 10.1140/epjc/s10052-010-1314-6. arXiv: 0906.
  1833 [hep-ph].
- [44] S. Tripathy, A. Bisht, R. Sahoo, A. Khuntia, and M. P. Salvan, "Event Shape and Multiplicity Dependence of Freeze-Out Scenario and System Thermodynamics in Proton+Proton Collisions at  $\sqrt{s} = 13$  TeV Using PYTHIA8," *Adv. High Energy Phys.*, vol. 2021, p. 8822524, 2021. DOI: 10.1155/2021/8822524. arXiv: 1905.07418 [hep-ph].

- [45] B. B. Abelev et al., "Performance of the ALICE Experiment at the CERN LHC," Int. J. Mod. Phys. A, vol. 29, p. 1430 044, 2014. DOI: 10.1142/S0217751X14300440. arXiv: 1402.4476 [nucl-ex].
- [46] J. Cleymans and D. Worku, "The Tsallis Distribution in Proton-Proton Collisions at  $\sqrt{s}=0.9$  TeV at the LHC," J. Phys. G, vol. 39, p. 025 006, 2012. DOI: 10.1088/0954-3899/39/2/025006. arXiv: 1110.5526 [hep-ph].
- [47] B. Abelev et al., "Pion, Kaon, and Proton Production in Central Pb-Pb Collisions at  $\sqrt{s_{NN}}=2.76$  TeV," Phys. Rev. Lett., vol. 109, p. 252 301, 2012. DOI: 10.1103/PhysRevLett.109.252301. arXiv: 1208.1974 [hep-ex].
- [48] G. Aad et al., "Charged-particle multiplicities in pp interactions measured with the ATLAS detector at the LHC," New J. Phys., vol. 13, p. 053 033, 2011. DOI: 10.1088/1367-2630/13/5/053033. arXiv: 1012.5104 [hep-ex].
- [49] V. Khachatryan et al., "Transverse-momentum and pseudorapidity distributions of charged hadrons in pp collisions at  $\sqrt{s} = 7$  TeV," Phys. Rev. Lett., vol. 105, p. 022 002, 2010. DOI: 10.1103/PhysRevLett. 105.022002. arXiv: 1005.3299 [hep-ex].
- [50] J. Cleymans, G. I. Lykasov, A. S. Parvan, A. S. Sorin, O. V. Teryaev, and D. Worku, "Systematic properties of the Tsallis Distribution: Energy Dependence of Parameters in High-Energy p-p Collisions," *Phys. Lett. B*, vol. 723, pp. 351–354, 2013. DOI: 10.1016/j.physletb. 2013.05.029. arXiv: 1302.1970 [hep-ph].
- [51] G. Bıró, G. G. Barnaföldi, and T. S. Biró, "Tsallis-thermometer: a QGP indicator for large and small collisional systems," J. Phys. G, vol. 47, no. 10, p. 105 002, 2020. DOI: 10.1088/1361-6471/ab8dcb. arXiv: 2003.03278 [hep-ph].
- [52] E. Schnedermann, J. Sollfrank, and U. W. Heinz, "Thermal phenomenology of hadrons from 200-A/GeV S+S collisions," *Phys. Rev.*

- C, vol. 48, pp. 2462-2475, 1993. DOI: 10.1103/PhysRevC.48.2462.
  arXiv: nucl-th/9307020.
- [53] T. Csorgo, S. V. Akkelin, Y. Hama, B. Lukacs, and Y. M. Sinyukov, "Observables and initial conditions for selfsimilar ellipsoidal flows," *Phys. Rev. C*, vol. 67, p. 034 904, 2003. DOI: 10.1103/PhysRevC.67. 034904. arXiv: hep-ph/0108067.